# Preparation and Characterisation of $Na_2Fe_2(MoO_4)_3$ Solid Solution as Potential Cathode Material in Sodium-Ion Batteries

**Moyana Constatia**

**Student number: 14000229**

Dissertation submitted for Master of Science Degree in Chemistry

Faculties of Sciences, Engineering and Agriculture

University of Venda

Thohoyandou, Limpopo

South Africa

Supervisor: Dr Legodi M.A Signed: ……Date: …10/06/2022……………

Co-supervisor: Prof Teuns van Ree Signed: .Date: 29/05/2022

Co-supervisor: Dr Sikhwivhilu L.M Signed: ….Date: …10/06/2022…………

# Dedication

Dedicated to my son, Phumudzo Themeli. To my Mother and Grandmother, Lavani Asnath Maluleke & Mamaila Sarah Ramantswana, and my siblings, Vutomi, Mapule, Mpho, Mulalo & Tshifhiwa, for their endless love, support and encouragement.

# Declaration

I, Moyana Constatia, student number: 1400229 declare that this dissertation is my original work and has not been submitted for any other degree at any other university or tertiary institution. The dissertation does not contain any other person's writings unless specifically acknowledged and referenced accordingly.

Signed (Student): Date: 22/02/2022

# Acknowledgements

Firstly, I would like to give thanks to the almighty God for providing me with good health and inspiration during the research period.

Secondly, thanks to my supervisor Dr Legodi M.A. for his support, guidance and critical comments that he has provided throughout my research work, together with my co-supervisors Prof. van Ree T. and Dr Shikhwivhilu L.

Lastly, I would like to express my appreciation to my family together with Mpho Mudau and Tshikhudo Fulufhelo for their encouragement and support throughout my research.

# Abstract

$Na_2Fe_2(MoO_4)_3$ is a good cathode material for sodium storage due to its low cost, non-toxicity of iron and three open dimensional crystal framework. $Na_2Fe_2(MoO_4)_3$ was synthesised using the one pot sol-gel method. $Na_2Fe_2(MoO_4)_3$ was then doped using chromium, zinc, copper, calcium and potassium to improve electrochemical performance. A sol-gel method was used to synthesise $Na_2M_yM_xFe_{2-x-y}(MoO_4)_3$ (where $0 \leq x \leq 0.5, 0 \leq y \leq 0.5$). A weakness of the synthesis method used was that it was not viscous. The presence of lead and sulphur which should not be part of the product is due to the use of iron sulphate as a source of iron. The presence of lead seems to be due to the contamination of the cathode material. The synthesized materials were calcined at 600 °C for 3 hours to produce the desired material as shown by the elemental distribution. The synthesised material was characterised by XRD, XRF, SEM-EDS, FTIR and Raman spectroscopy. The synthesis of $Na_2Fe_2(MoO_4)_3$ was successful because the FTIR spectra shows the observed bands of 1674.13 $cm^{-1}$ for metal oxide (Na-O),1429.75 $cm^{-1}$ due to (C-O),567 $cm^{-1}$ due to (Fe-O) and 814.77 $cm^{-1}$ due to (Mo-O), XRF shows relative the composition of the sample is Fe= 9.543 and Mo= 44.003.The SEM micrographs reveal that the morphology consists of a smooth surface with irregular shapes and particle size is approximately 1 μm. The XRD parent and doped samples present nine characteristic peaks at 13.87, 22.05, 25.60, 29.15,34.64 and 55.62° corresponding to the crystal planes 200, 311, 212, 124,420 and 0.108. Using stoichiometric amounts of reactant, $Na_2Fe_2(MoO_4)_3$ was doped at the Fe site and the Na site was successfully synthesised using a one pot sol-gel synthesises method followed by calcination in the presence of air for 3 hours at 600 °C

Keywords:
$Na_2Fe_2(MoO_4)_3$, Doping, sodium-ion, Cathode, Battery, spectra.

# Abbreviations and Acronyms

BES - Battery Energy Storage

DDB – 1,4-di-tert-butyl-2-5-dimethoxybenzene

DFT - Density functional theory

FTIR – Fourier transform infrared spectroscopy

LIBs – Lithium-ion battery

$Na^+$ - Sodium-ion

NASICON - Sodium super ionic conductor

PC - Propylene carbonate

SEI - Solid electrolyte interphase

SEM-EDS – Scanning electron microscopy – energy dispersive spectroscopy

SIB - Sodium-ion battery

TPA – Triphenylamines

TAC - Trisaminocyclopropenium

TAC.ClO4 – Trisaminocyclopropenium perchlorate

UPS - Uninterruptible power supply

XAS - X-ray absorption spectroscopy

XRD - X-ray diffraction

XRF – X-ray fluorescence

# Table of Contents

# List of Figures

SEM micrograph from Figure 4.7 to Figure 4.12

# List of Tables

# Chapter 1: Introduction

“The demand for sodium ions rechargeable batteries(SIBs) will continue to rise as renewable energy sources are integrated into the electrical grid, and electric vehicles continue to be developed” (Erickson *et al*., 2014). “Sodium-ion batteries are promising alternative to lithium-ion batteries due to the low cost and abundance of sodium element in the earth. The chemical similarity of this sodium ion to lithium-ion enables some electrode materials used in Li-ion batteries (LIBs) to be applied for SIBs” (Ellis *et al*., 2012). Sodium-ion electrode material can be used in applications using large-amount of energy storage like smart grids and solar/wind energy systems. The low cost of sodium material will reduce the challenge related to their synthesis. (Slater *et al*., 2013).

## 1.1 What is a battery?

A battery is an electric current-producing electrochemical cell or set of cells. Any galvanic cell might theoretically be used as a battery. A perfect battery will never run out of power, must produce constant voltage, and be able to tolerate temperature and humidity extremes. Real batteries strike a balance between ideal performance and realistic constraints. An automobile battery, for example, weighs roughly 18 kg, or about 1% of the mass of a typical car or light-duty truck. If employed in a smartphone, this type of battery may provide practically limitless energy, but it would be rejected due to its size. As a result, no single battery is "best," and batteries are chosen for specific applications based on factors such as the battery's mass, cost, reliability, and current capacity. Primary and secondary batteries are the two basic types of batteries. We will now briefly discuss a few examples of each sort of battery.

Each sodium ion battery consists of three components: cathode (positive electrode), anode (negative electrode) and electrolytes containing sodium salts.

## 1.2 Battery categories

### 1.2.1 Primary Batteries

Primary batteries are non-reusable and are used once and then thrown away. They have the advantage of being more convenient and costing less per battery, but they also cost more in the long run. Primary batteries have a sloping discharge curve and a higher capacity and beginning voltage than rechargeable batteries. Currently, most basic batteries do not require specific disposal.

#### 1.2.1.1 Advantages of primary batteries

- There are no design compromises required to accommodate recharging, resulting in a high energy density.
- They are the best option for low-cost, low-power applications like watches or hearing aids.
- Primary batteries are the logical choice for single-use applications such as guided missiles and military weapons.
- Production has low start-up costs
- Convenient to use
- The wide availability of standard products

#### 1.2.1.2 Shortcomings of primary batteries

Because of the limited lifetime and the cost of continual replacement, it is not appropriate for high-drain applications.
Single-use, disposable main batteries are a very inefficient energy source in terms of overall energy efficiency, producing just approximately 2% of the power needed in their creation.
They also generate a significant amount of waste when compared to rechargeable batteries.

### 1.2.3 Secondary Batteries

Various rechargeable secondary batteries are available. These are the batteries that go into electronics like smartphones, electronic tablets, and cars.

NiCd batteries have a nickel-plated cathode, a cadmium-plated anode, and an electrolyte of potassium hydroxide. The divider keeps the positive and negative plates from shorting, so they're rolled up and put in the case together (Paul *et al* 1968). The NiCd cell's "jelly-roll" structure allows it to deliver significantly more current than an alkaline battery of equal size used in battery manufacturing. The establishment of reused material criteria has been highlighted as a strategy for the advanced battery manufacturing business to improve the utilization of recycled material (Shoesmith *et al*., 2007)

In rechargeable batteries used in consumer and hybrid electric vehicle applications, lithium-ion and nickel-metal hydride chemistries (also known as "advanced batteries") are used. In its current state, the advanced battery sector rarely produces batteries from recycled materials (Ziegler *et al*., 2021). Today's technology for used battery decommissioning and material recovery is based on pyrometallurgy and hydrometallurgy, which essentially burn, melt or dissociate advanced materials to recover metals for high strength alloys and other cobalt market areas. The diversification of the battery chemistry business may reduce the recoverable value of metals in reuse operations (Mohammed et al., 2020).

The diversification of the storage chemistry market may reduce the recoverable value of metals in the recycling processes used today. Soft chemical or green chemical-based processing is available, allowing for the recovery of advanced materials (Espinosa et al., 2012)

In rechargeable metal-ion batteries, positive electrode material, which is the cathode, undergoes “reversible intercalation, displacement or conversion processes to store electricity” (Palomares *et al*., 2012). The sodium and lithium positive intercalation electrodes are made of layered oxide, spinel oxide, or polyanionic compounds (Wang *et al*., 2015). In recent years, more attention has been paid to the analysis of metal oxides containing mobile lithium ions due to their high application potential in the fields of energy and electronics. Metal oxides such as $LiMO_2$ (M = Mn, Fe, Co, Ni) (Whittingham & Silbernagel, 1976; Mizushima *et al*., 1980; Kanno *et al*., 1994), which can be used in the fabrication of high energy density electrochemical generators have been studied.

The electrolytes enable the transfer of sodium ions between the electrodes as illustrated by Figure 1.1. The electrolytes are in the porous separator membrane that prevents contact between the anode and the cathode (John *et al*., 2014). When the battery is charged, the cathode releases some of its sodium ions, which move through the electrolyte until they reach the anode where they are stored in form of chemical energy. When the battery is discharged and used up, the stored sodium ions are released from the anode. The anode releases some of its sodium ions which move through the electrolyte and are stored back at the cathode as shown by Figure 1.1 this type of process happens all the time during charging and discharging (Yang, 2018).

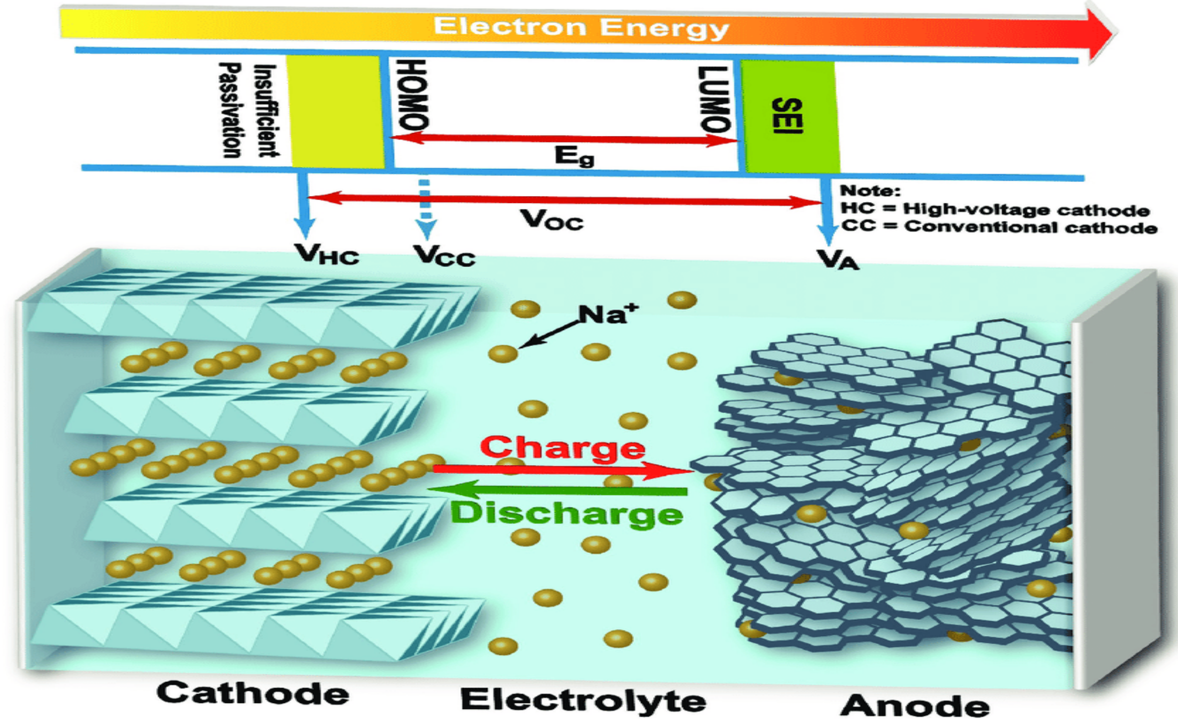

**Figure1.1**: The charging and discharging process in a sodium-ion battery with the electrolyte between anode and cathode (Xiaolin, *et al*., 2020).

The electrolyte of SIBs must be carefully selected to offer strong resistance in the redox environment at anodic and cathodic sites. The electrolyte must be inert and remain stable over a long range of temperatures. The electrolyte in the majority of SIBs is a sodium salt dissolved in an organic solvent (Xu, 2004). The most common electrolyte formula for sodium batteries is $NaPF_6$ or $NaClO_2$ as a salt dissolved in carbonate ester solvents, especially propylene carbonate (PC). In the presence of the organic electrolytes used, metallic sodium anodes rust continuously. They corrode instead of forming a stable solid electrolyte interphase (SEI) (Michael, 2013). Strongly reducing sodium-containing intercalation compounds intended for use as an anode may also require tailored SEIs to enable stable cycling in the cell. Discharged product impurities such as sodium propyl carbonate are generated on the Na anode surface in reaction with PC. PC is the most commonly used solvent in $Na^+$ ion batteries, serving as the base in roughly 60% of the electrolyte formulations in the SIB literature (Ponrouch *et al*., 2012). This species can be oxidized at the cathode when fully charged, limiting capacity utilization and causing coulombic inefficiency. To ensure field success, the formulations and conditions required for proper SEI formation must be developed along with the anode material (Hong *et al*., 2018). There is still a lot of research to be done on solvents, Na-supporting electrolyte salts, and additives, as well as understanding the reaction mechanisms and enabling stable cycling properties (Michael *et al*., 2013)

## 1.3 Importance of batteries in everyday life (www.Eurobat.org) (2021)

Batteries perform a wide range of functions in everyday life, from providing the initial energy needed to start car engines to functioning as a backup power source in telecommunications, public transportation, and medical treatments. Batteries can reduce greenhouse gas emissions by storing electricity from conventional and renewable energy sources and serving as a power source for electric vehicles (Eurobat, 2021).

Battery Energy Storage (BES) can assist the globe in transitioning to a more sustainable and secure energy system based on renewables, thereby lowering greenhouse gas emissions and enhancing energy independence. Batteries can store energy from on-peak renewable energy and release it when it's needed the most in centralized, decentralized, and off-grid situations. Voltage control and frequency regulation are two grid support services that batteries can provide, assuring grid stability and flexibility. Overall, batteries have the potential to improve the world's renewable energy utilization, as well as its energy efficiency, sustainability, independence, and security, batteries can be used at every level of the power grid:

- Batteries can store energy produced with renewables that could not be fed into the grid and would have been curtailed at the generation level. Furthermore, the combination of variable renewable power and energy storage offers a fixed generation capacity that can be valued on capacity markets. Batteries can also help grid stability by compensating for the destabilizing effects of variable generation.

- At the transmission and distribution levels, batteries can provide a variety of auxiliary services to help stabilize the energy grid by improving operating conditions, increasing capacity, and making it more secure, dependable, and responsive. Batteries have the ability to store or inject energy swiftly into a grid area, even in milliseconds, to minimize frequency instability. Batteries can supply grid reserve capacity to replace the spinning reserves provided by traditional rotating generating units.

- A battery system connected to a PV or small wind generator can enhance the quantity of self-produced electricity as well as self-consumption at the household level. Furthermore, batteries can reduce the distortion induced by inverters, allowing for more efficient grid injection. Presumes can also provide grid operators with supplementary services, which can be aggregated and managed by third parties. As an uninterruptible power supply unit, BES can support client loads and provide backup power for the duration of a power outage (UPS).

## 1.4 Impact of batteries in the environment

Batteries are a ubiquitous part of modern life. They're used for a variety of things, including:

- Transportation:

Cars, planes, electric bikes, trains, and a variety of other applications for the transportation of goods and people, such as forklift trucks and wheelchairs, use lithium-ion batteries.

- In both hybrid and all-electric cars
- Renewable energy technologies require energy storage.
- Uninterruptible Power Supply (UPS), security, telecommunications, power plants, computer systems, airlines, trains, metros, and tunnels all require backup power.
- Applications in industry and the military.

These examples demonstrate the importance of batteries in everyday life. We want consumers to trust batteries not only in terms of their everyday use but also in terms of the environmental precautions built into their design. To ensure that the highest environmental protection criteria are met, by controlling every stage of a battery's life cycle, from design and production to their varied uses and applications, to final collection and recycling. Batteries can aid in the reduction of $CO_2$ emissions.

## 1.5 Problem statement

As renewable energy sources are integrated into the electrical grid and electric vehicles continue to be developed, the demand for rechargeable sodium-ion batteries will grow. (Erickson *et al.*, 2014). One of the hurdles in commercialization of SIBs is the lack of suitable cathode materials $Na_2Fe_2(MoO_4)_3$ is promising cathode material for both $Li^+$ and $Na^+$ ion batteries owing to its highly reversible accommodation of intercalated ions. There are many promising cathode materials to power the transportation system efficiently, but none are ideal as they have questionable safety, poor cyclability, slow sodium insertion and low electrical conductivity.

The search for a better cathode material from a high abundance of resources, at better cost and safety, continues. Sodium-ion batteries show high-temperature Na-S batteries, high density and high power. They have attracted rapidly increasing attention. $Na_2Fe_2(MoO_4)_3$ is investigated as highly promising cathode material due to its low cost and abundance of sodium metal. In this study doped derivatives of $Na_2Fe_2(MoO_4)_3$ are synthesised by the sol-gel method. Single and double doping $Na_2Fe_2(MoO_4)_3$ will be investigated to improve the electrochemical properties.

## 1.6 Rationale of the study

This work is part of a broad sodium-ion battery study. Electrode materials have been synthesized for sodium and lithium-ion batteries but new markets are placing high demands for innovative materials. Sodium iron molybdates reportedly have excellent properties and few drawbacks. $Na_2Fe_2(MoO_4)_3$ has good electrochemical properties, but poor cycle stability and slow insertion and low electric conductivity limit its application. Amongst all the safety issues of SIBs overcharge is the only issue that can induce particularly harsh thermal runaway.

During overcharge, sodium dendrites grow at the anode surface and the cathode structure will then collapse, this process then causes a series of side reactions that generate heat and gas and eventually evolve into disastrous thermal runaway, discussed in chapter 2. The rationale for the synthesis of new doped $Na_2Fe_2(MoO_4)_3$ is to improve the sodium-ion batteries' performance.

## 1.7 Aim

- To synthesise and characterise doped $Na_2Fe_2(MoO_4)_3$ solid solutions for use as electrode materials in sodium-ion batteries

## 1.8 Objectives:

- To dope $Na_2Fe_2(MoO_4)_3$ introducing (Cr, Zn, and Cu) at the Fe sites with the sol-gel method
- To dope $Na_2Fe_2(MoO_4)_3$ using (K and Ca) at the Na sites with the sol-gel method

- To characterize products using, FTIR, XRD, XRF, Raman spectroscopy and SEM-EDS
- To investigate the effects of metal doping on the physical and chemical properties of $Na_2Fe_2(MoO_4)_3$

## 1.9 Hypothesis

Doping is expected to influence the structure, morphology, crystallinity and chemical properties of $Na_2Fe_2(MoO_4)_3$. The method is expected to have a great influence on the properties of the material, decomposition temperature and particle size of the samples. This will, in turn, have a great influence on the electrochemical performance of the cathode materials used in rechargeable sodium-ion batteries

## 1.10 Research outline

1. Introduction

It includes the battery categories, advantage of primary batteries, shortcomings of primary batteries, importance of batteries in everyday life, Impact of batteries in the environment, Problem statement, rational of the study, aim, objectives and hypothesis.

2. Literature review

It contains Sodium ion battery, SIB drawbacks and remedies, review of some of the previously synthesized material, sodium electrolyte interphase(SEI) in sodium-ion batteries, Meaning of SEI and its importance, Overcharge protection, toxicity of SIBs and literature synthesis methods.

3. Experimental

General experimental conditions, experimental and instrumental analysis

4. Results

This chapter discuss about the characterisation results such as x-ray diffraction, Raman spectroscopy, Scanning electron microscopy, energy dispersive x-ray spectroscopy, Fourier transform infared spectroscopy and x-ray fluorescence spectroscopy.

5. Conclusion

It contain the summary of the whole research

6. References

Some of the used, books, journal and publication.

# Chapter 2: Literature review

## 2.1 Sodium-ion batteries

Many materials for rechargeable batteries have been developed in recent decades, and low-cost electrical energy storage is now a global priority in a wide range of scientific and technological research (Hoffert *et al*., 2002). To wean ourselves off our reliance on non-renewable energy sources, society has responded to the dilemma by innovating battery technology, particularly lithium-ion batteries (Kang and Cedar. 2001). After decades of effort, LIBs have infiltrated our daily lives, and the expansion of LIBs is expected to continue at an increasing rate (Tarascon and Armand. 2001). The cost of batteries in various applications has been the game changer as they transition from portable consumer devices to grid-scale electric energy storage and electric automobiles (Tarascon and Armand. 2008). As a result, LIB development is dependent on the market price of the lithium material, and replacing lithium with less expensive alternatives could result in future batteries being subject to price volatility as the market grows (Lu and Li., 2013).

SIBs and LIBs, rely on the "reversible migration of cations/anions across a separator toward the electrodes to achieve voltage-driven electrochemical reactions" (Zhao *et al*., 2013). In fact, SIBs and LIBs emerged around the same time in the 1980s, but LIBs eventually overtook SIBs because of their superior electrochemical properties (Dannel *et al*., 2011).

## 2.2 SIB drawbacks and remedies

A major stumbling block is obtaining a sodium host material with similar operating voltage and capacitance as the LIB analogy.

- To begin with, the greater $Na^+$ radius (0.098 nm) than Li+ (0.069 nm) causes kinetically sluggish $Na^+$ insertion/extraction and transit through the host-material framework, resulting in largely impaired specific capacity and rate capacity (Peters *et al*., 2016).
- Second, compared to LIB equivalents, the higher volume expansion due to Na+ injection would create a change in the state and lattice of the host materials, making it difficult to obtain acceptable electrochemical stability (Islam *et al*., 2014).
- Lastly, due to the smaller potential and higher atomic weight of sodium, they have lower specific energy than LIBs.

- Building a cheap Na-host material with high specific energy (e.g., 500 W-h kg$^{-1}$ in LIBs) remains a difficulty (Kundu *et al*., 2015). Unlike LIBs, which must be shipped with 20-40% state of charge to avoid copper dissolution, SIBs can be stored in the short-circuit state, which poses less of a safety concern during shipment and storage (Yabuuch *et al*., 2014)

According to this study, cathode materials should not only account for a higher percentage of a sodium-ion battery's weight, but they also hold more promise for improving SIB voltages (Pan *et al*., 2013). Advanced cathode resources with high specific energy, high-rate performance, excellent cycling stability, and good safety continue to be highly sought after (Zhengfei *et al*., 2017). Layered metal oxides, phosphates, pyrophosphates, NASICON-based compounds, fluorides, and organic compounds are some of the basic properties of SIBs, as well as the special qualities inherent in existing SIB cathodes, as shown in Figure 2.1 (Zhengfei *et al*., 2017).

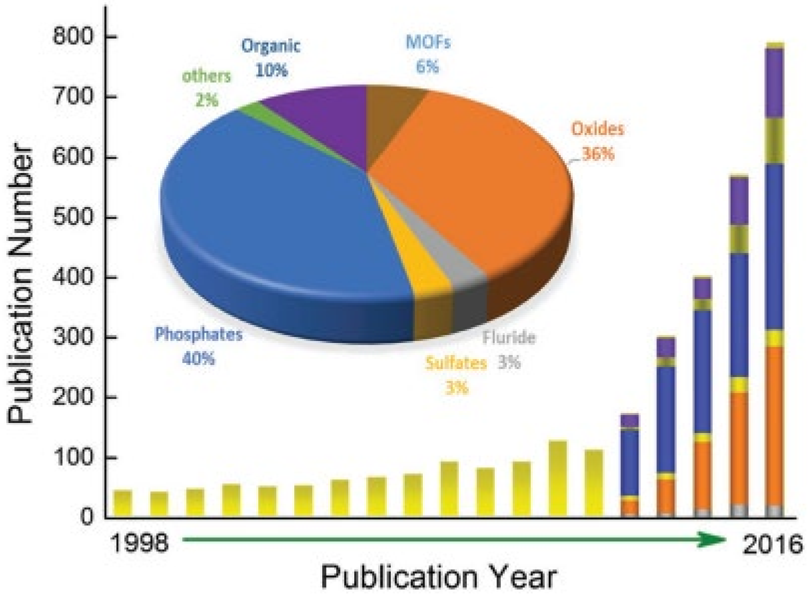

**Figure 2.1** “Histogram and bar chart showing the number of publications regarding cathodes for SIBs annually and in different materials systems” (December 15, 2016).

The predicted formation energy of a $VO_2$ molecule is plotted against the quantity of sodium ions in the molecule in Figure 2.2. The greater negative production energy shows the creation of the more inert phase when the injected sodium ions increase from 0 to 1. When the concentration of Na ions x exceeds 1, however (e.g., $Na_{1.25}VO_2$), when compared to $NaVO_2$, the related formation energy y is higher, with a severe Na-insertion-induced volume expansion and broken V–O tunnels (Figure 2.2 (b)).

As a result, the Na-insertion process (discharge process) from the $VO_2$ phase to the stable $NaVO_2$ phase might occur spontaneously. As a result, Figure 2.2 (c) depicts the transition of the Na ions during the charge and discharge process.

In the first discharge step, one Na ion is injected into a $VO_2$ molecule to generate the $NaVO_2$ phase, which is subsequently oxidized to $Na_xVO_2$ in the subsequent charging process. The theoretical capacity of $VO_2$ is calculated to be 323 mA-hg$^1$ using the single-Na-insertion method.

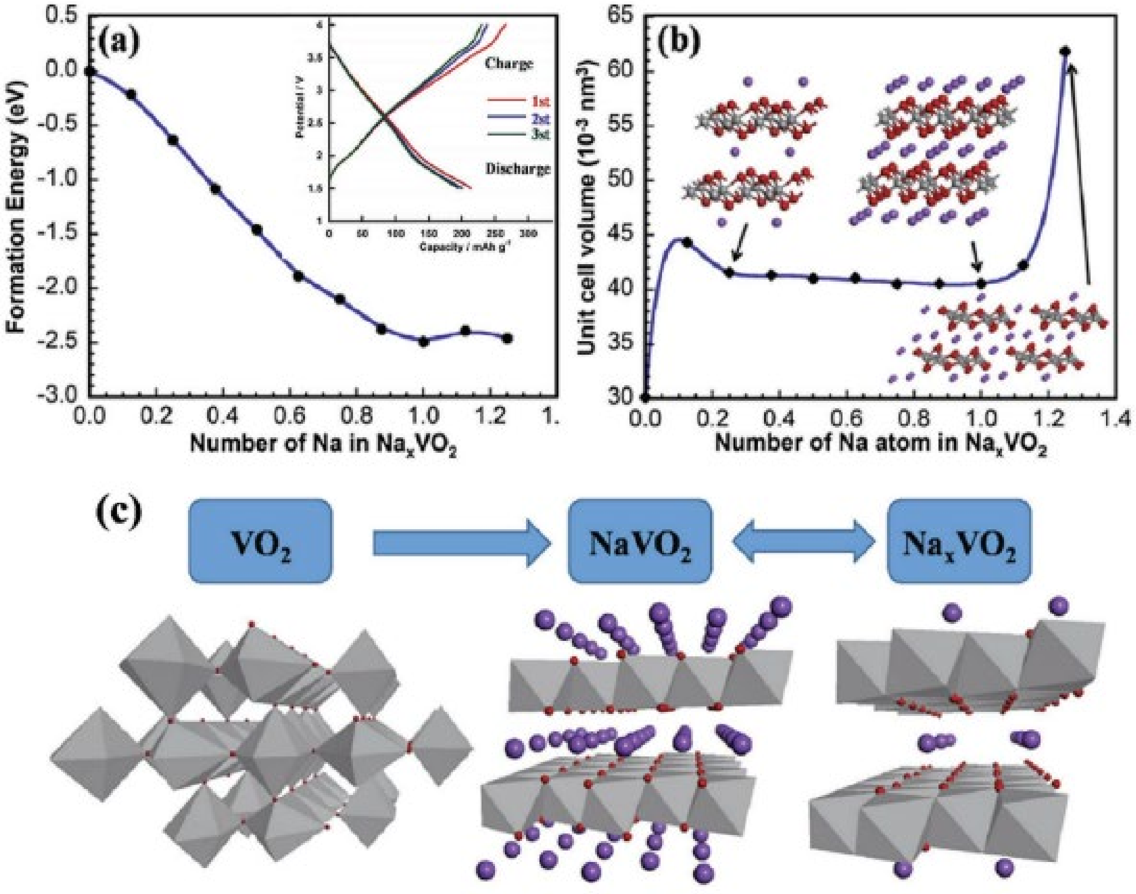

**Figure 2.2** The predicted formation energy of a $VO_2$ molecule is plotted against the quantity of sodium ions in the molecule (Kim *et al*., 2012).

Vanadium pentoxide is divided into two forms based on its crystal structure: orthorhombic $V_2O_5$ and bilayered $V_2O_5$. The layered structure of $V_2O_5$ allows for easier insertion and extraction of Na-ions. The electrochemical performance of bilayered $V_2O_5$ with a larger d-spacing than orthorhombic $V_2O_5$ as a cathode material in Na-ion batteries has been reported.

Figure 2.3: "Illustrates the various crystal structures of sodium inserted-transition metal oxides. The $O_3$-phase and $P_2$-phase are the most popular structural polymorphs of layered metal oxides serving as cathodes for SIBs'' (Kim *et al*., 2012). "$Na^+$ ions can be reversibly inserted and deinserted between the $(MO_2)_n$ layers formed by edge-shared $MO_6$ octahedra. Air stability is one of the key issues in layered oxide cathodes. Although $O_3$-type oxide cathodes can deliver higher reversible specific capacities, they still suffer from weak air stability as well as poor cycling stability. In contrast, $P_2$-type compounds can have better cycling stability and air stability due to their larger trigonal prismatic sites occupied by $Na^+$ ions, which is helpful for the transport of $Na^+$ ions"(Zhengfei *et al*.,2017)

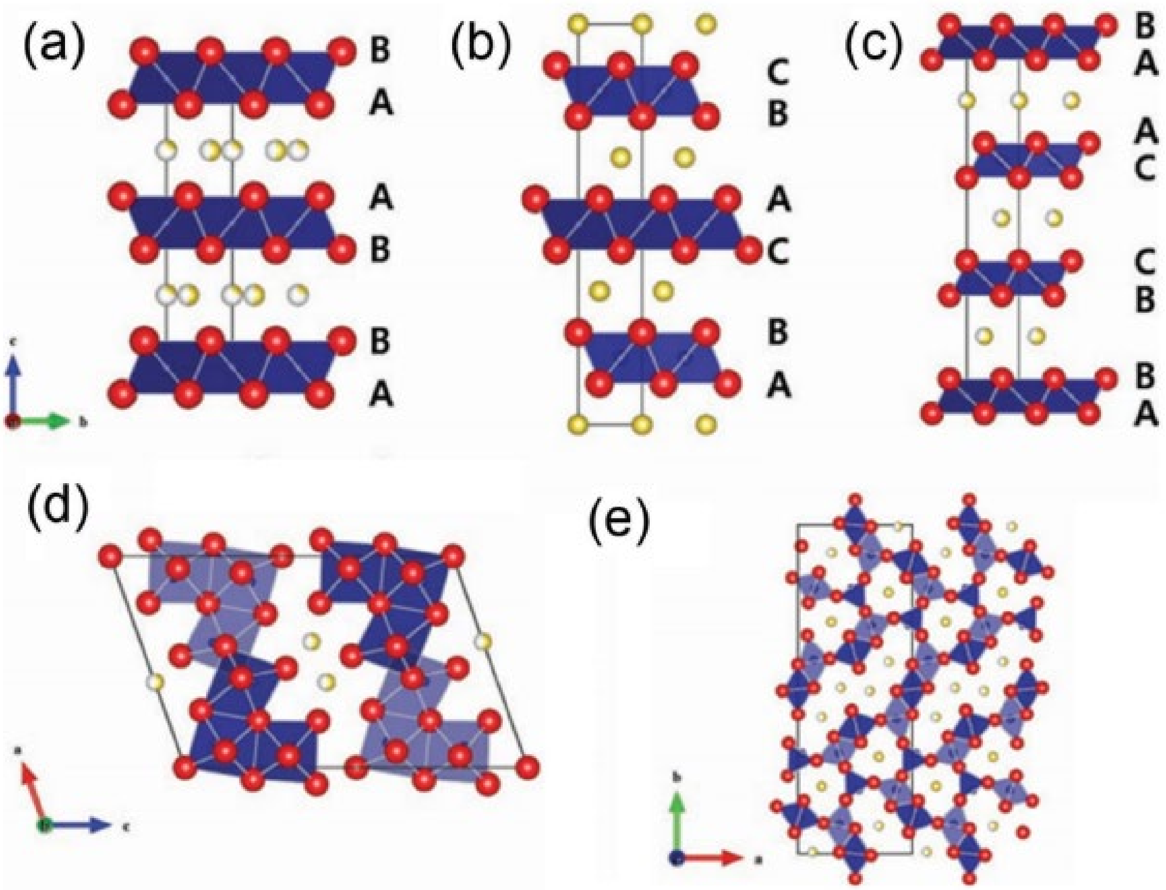

**Figure 2.3** Crystal structures of various $Na_xMO_y$: a) $P_2$-$Na_xCoO_2$, b) $O_3$-$Na_xCoO_2$, c) $P_3$-$Na_xCoO_2$, d) $Na_{0.44}MnO_2$, and e) $Na_{0.33}V_2O_5$ (Na: yellow, Co/Mn/V: blue, O: red)(Kim *et al*., 2012).

The On (n = 1, 2, 3, etc.) symbolises structures in which Na is octahedrally coordinated by oxygen with a repeated period and of metal stacking, while Pn represents structures in which Na occupies trigonal prismatic sites (Zhengfei *et al*., 2017).

With an initial discharge capacity of 195 mA h g1 at 0.1C and increased cycling stability of 86.4% over 80 cycles, electrospun $P_2$-$Na_{2/3}(Fe_{1/2}Mn_{1//2})O_2$ hierarchical nanofibres demonstrated remarkable electrochemical performance in SIBs. “An air-stable and Co/Ni-free $O_3$-$Na_{0.9}[Cu_{0.22}Fe_{0.30}Mn_{0.48}]O_2$ cathode (2.5 - 4.5V) recently demonstrated an energy density of 210 W-h kg1, a high round-trip energy efficiency of 90%, and excellent cycling stability, whereas the control sample, $O_3$-$NaFe_{1/2}Mn_{1/2}O_2$, is not stable with water and shows relatively large polarization in the charge and discharge curves” (Park *et al*., 2015).

To improve electrochemical performance, even more, ternary and quaternary metal oxide cathodes have been studied extensively in recent years. Hasa *et al*. conducted a $P_2$-type

$Na_{0.5}[Ni_{0.23}Fe_{0.13}Mn_{0.63}]O_2$ layered material for SIB cathodes that showed good electrochemical performance in terms of cycle response and delivered capacity, including high capacity extending up to 200 mA h g1 throughout the 4.6 - 1.5 V voltage range.

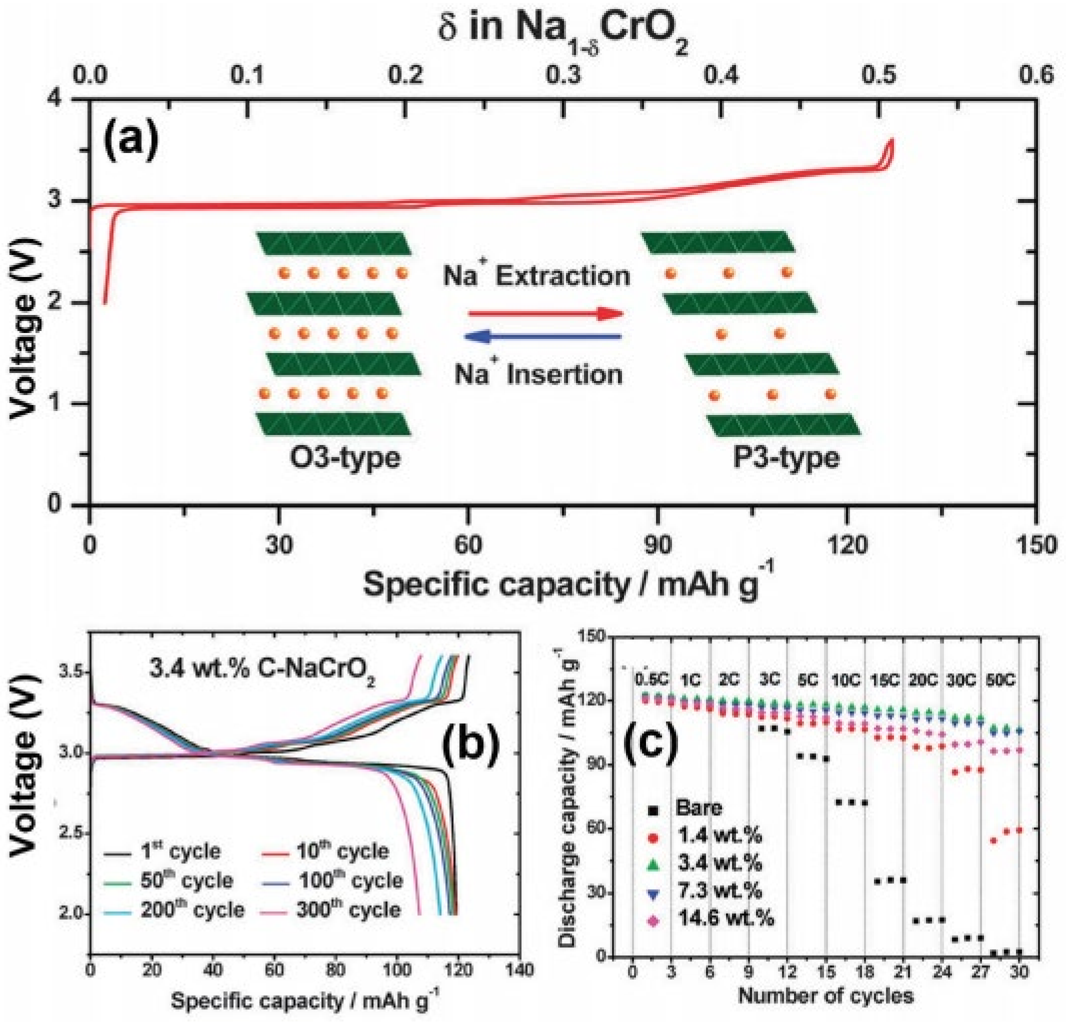

**Figure 2.4** “First charge-discharge curve with a schematic of the $NaCrO_2$ phase transition. b) Charge–discharge curves up to 300 cycles of the 3.4 wt% carbon-coated electrodes. c) Rate capability as a function of the amount of carbon contained” (Park *et al.*, 2015).

## 2.3 Review of some previously synthesized materials

### 2.3.1 $Na_2Fe_2(MoO_4)_3$ (www.nature.com)

$Na_2Fe_2(MoO_4)_3$ is a promising cathode resources for $Li^+$ and $Na^+$ ion batteries due to its high reversible uptake of intercalated ions (Mathiram *et al*., 1987). $Fe_2(MoO_4)_3$ crystallises in a thermodynamically favored low-temperature monoclinic structure ($P2_1/c$) composed of $FeO_6$ octahedra and $MoO_4$ tetrahedra connected by corner-sharing oxygen atoms (Bruce *et al*., 1990). The structure's basic motif is called the "lantern unit," and it is made up of three $MoO_4$ tetrahedra that connect two $FeO_6$ octahedra (Nadiri *et al*., 1984). In the anti-NASICON material, these units stack antiparallel along the (2b+c) axis. The equivalent units of the NASICON structure stack in parallel along the c-axis (Masquelier *et al*., 2013).

"Two isostructural iron molybdates $NaMFe(MoO_4)_3$ ($M$ = Ni, Zn) have been prepared as single crystals by flux method" (Mhiri *et al*., 2016). Both compounds ($NaNiFe(MoO_4)_3$ and $NaZnFe(MoO_4)_3$ ) crystallise in the triclinic system with the space group P-1 and Z = 2. The ionic conductivity results insert good ionic conductivities with low activation energies similar to those of NASICON type compound with formula $AZr_2(PO_4)_3$ (A = Na, Li) (Mhiri *et al*., 2016).

"The electrochemical performance of $Li^+$ and $Na^+$ (de)insertion into $Fe_2(MoO_4)_3$ has been previously studied. The existing information in the literature is often contradictory, and the mechanism of structural transformations from the parent phase to the intercalated phase remains unknown for monoclinic $Fe_2(MoO_4)_3$. Nadiri *et al.* (1984) reported a single-phase structural change in monoclinic $Fe_2(MoO_4)_3$ during $Na^+$ (de)insertion in the composition ranges of $0.3 \le x \le 1.0$ and $1.10 \le x \le 1.60$ for $Na_x Fe_2(MoO_4)_3$ (Nadiri *et al*., 1984). In contrast, Bruce *et al*. (1990) reported the presence of two phases throughout the composition range $0 < x < 2$ through *ex situ* x-ray diffraction" (researchportal.bath.ac.uk)

"Up to now six orthomolybdate compounds have been reported in the Na-Fe-Mo-O systems: $Na_9Fe(MoO_4)_6$ (Savina *et al*., 2013); $NaFe(MoO_4)_2$ (Klevtsova, 1975); $NaFe_2(MoO_4)_3$, $NaFe_2(MoO_4)_3$ and $Na_3Fe_2(MoO_4)_3$ (Muessig *et al.,* 2003); $NaFe_4(MoO_4)_5$ (Ehrenberg *et al*., 2006). The above-mentioned structures are described in terms of three-dimensional networks of isolated ($MoO_4$) tetrahedral and ($FeO_6$) octahedra. The $NaFe_2(MoO_4)_3$ and mixed-valence iron molybdate exhibits two polymorphs, both crystallising in the triclinic system. The low-temperature theta phase changes at high temperature into a beta phase" (docksci.com)

### 2.3.2 $Na_xFe_2(MoO_4)_3$

There is some indication (Figure 2.5) of a two-phase reaction taking place during the intercalation/deintercalation of both $Na^+$ and $Li^+$ into the monoclinic $Fe_2(MoO_4)_3$ (Sun *et al*., 2012), whereas single-phase solid solution reaction of $Na_xFe_2(MoO_4)_3$ ($0<x<2$) was also observed (Nadiri *et al*., 1984). This could be because of the structural complexity or the thermodynamic unfavorability of monoclinic $Fe_2(MoO_4)_3$ (Mantiram *et al.,* 1997). Orthorhombic $Fe_2(MoO_4)_3$ has been studied as a cathode material for lithium and sodium batteries. Its electrochemical properties and structural change behaviour during charging and discharging processes were studied by synchrotron-based X-ray diffraction (XRD), X-ray absorption spectroscopy (XAS), and aberration-corrected scanning (Shirikana *et al.,* 1997).

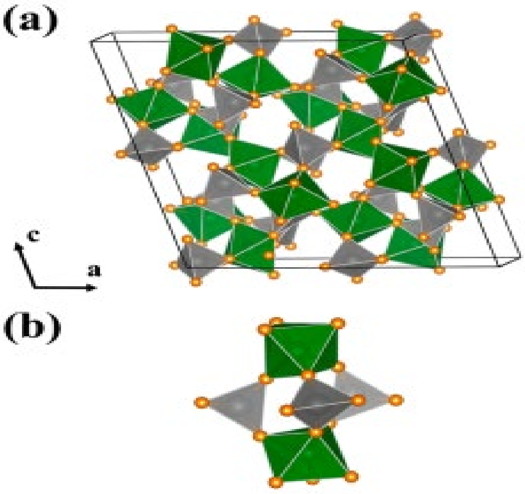

**Figure 2.5**: Showing the pristine monoclinic of $Fe_2(MoO_4)_3$ and lantern unit that consists of three $MoO_4$ tetrahedra connecting two $FeO_6$ octahedra.

“The XRD patterns of $Na_xFe_2(MoO_4)_3$ (x=0.0, 0.5, 1.0, 1.5 and 2.0) during the first discharge and charge cycle in a Na/$Fe_2(MoO_4)_3$ cell (Figure 2.6), show a completely different structural change behaviour other than those observed in lithium-ion cells ( Bruce *et al*., 1990). “No new set of peaks, but only peak shifts were observed throughout the entire discharge/charge process. During the discharge process, major peaks (111), (211), (102), (021), (310), (212), (022), (130) and (231) all gradually moved toward lower 2θ angles with increasing x from 0.0 to 2.0 in $Na_xFe_2(MoO_4)_3$. During the 6 recharge processes, all of these peaks reversibly moved back to their original positions with decreasing x from 2.0 to 0.0. The reversible peak shifts are attributed to the continuous lattice expansion and contraction during the discharge and charge processes respectively. This result demonstrates a typical single-phase (solid-solution) reaction during the discharge and charge process in the sodium cell" (Yue *et a*l., 2011).

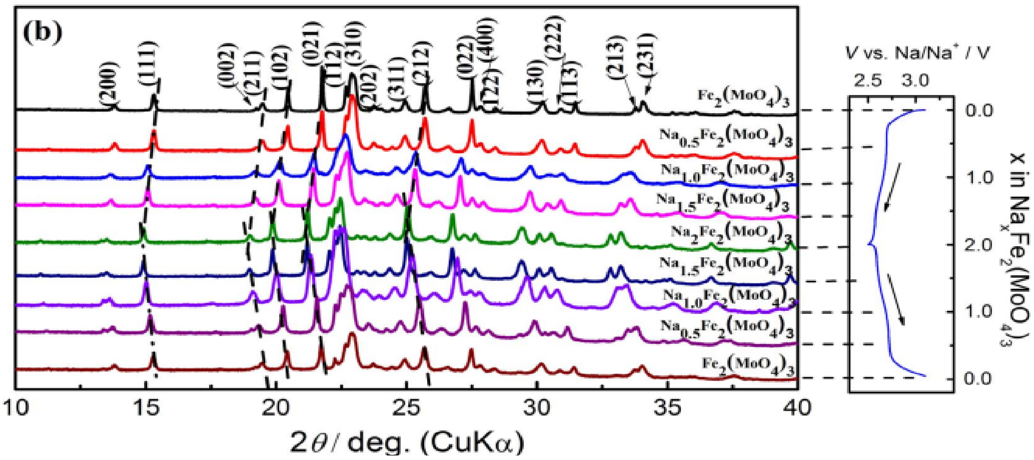

**Figure 2.6**: XRD pattern of $Na_xFe_2(MoO_4)_3$ at different concentrations. (Yue *et al.*, 2011)

It's worth noting that the same orthorhombic $Fe_2(MoO_4)_3$ structure exhibits such disparate structural change behaviours during the $Li^+$ and $Na^+$ intercalation/deintercalation processes (Dunn *et al.*, 2011). The crystal structure and thermodynamics of the orthorhombic $Fe_2(MoO_4)_3$ during guest alkali ion insertion have been studied. The crystal structure and thermodynamics of the orthorhombic $Fe_2(MoO_4)_3$ during guest alkali ion insertion have been investigated. The orthorhombic $Fe_2(MoO_4)_3$ crystal structure with space group Pbcn is made up of $MoO_4$ tetrahedra sharing all four corners with $FeO_6$ octahedra and $FeO_6$ octahedra sharing all six corners with $MoO_4$ tetrahedra. Such an open three-dimensional framework structure is suitable for the accommodation and diffusion of guest (A = Li and Na) ions. According to ab initio DFT calculations, the crystal structure of $Li_2Fe_2(MoO_4)_3$ after alkali ion intercalation is isostructural to $Na_xFe_2(MoO_4)_3$. The orthorhombic structure of $A_2Fe_2(MoO_4)_3$ (A = Li, Na) is the same as that of $Fe_2(MoO_4)_3$ (Meng *et al.*, 2011).

"The new compound $(Na_{0.4},Li_{0.6})(Fe,Li_2)(MoO_4)3$ was synthesized by cooling from the melt. Its anionic framework is built up from two distinct $MO_6$ octahedra, each containing disordered $Li^+$ and $Fe^{3+}$ ions in 0.6:0.4 and 0.7:0.3 ratios, and two $MoO_4$ tetrahedra, which link by vertex-sharing of their O atoms" (Souilem *et al.*, 2015). Nadiri *et al. (*1984) reported a single-phase structural change in monoclinic during $Fe_2(MoO_4)_3$ $Na^+$ (de)insertion in the composition ranges of $0.3 \le x \le 1.0$ and $1.10 \le x \le 1.60$ for $Na_xFe_2(MoO_4)_3$. In contrast, two phases were reported throughout the composition range of $0 < x < 2$ ex-situ X-ray diffraction of electrochemically intercalated powder samples. Recent studies by Yue *et al.* (2011) reported a two-phase structural change for $Li^+$ (de)insertion, but a single-phase process for $Na^{+-}$ intercalation in the high-temperature, the orthorhombic (not monoclinic) polymorph of $Fe_2(MoO_4)_3$. It is crucial to understand the mechanism by which the structural framework transform to accommodate guest ion intercalation, so that the contradictory report can be reconciled.

### 2.3.3 $NaMgFe(MoO_4)_3$

$NaMgFe(MoO_4)_3$ has been synthesised by the flux method (Mhiri *et al*., 2016). This compound is found to be isostructural with $NaFe_2(MoO_4)_3$ and it crystallises in the triclinic space group P1. The structure of molybdate is made up from $(Mg\text{-}Fe)_20_{10}$ units of edge-sharing $(Mg, Fe)O_6$ octahedra that are linked to each other through the common corners of $[MoO_4]$ tetrahedral (Bramnik *et al*., 2003). $Na^+$ cations are located in the anionic three dimensional framework that lead to formation of channels along its direction (Mhiri *et al*., 2016).

### 2.3.4 $Li_2Ni_2(MoO_4)_3$

Recently, the high voltage redox behaviour of the lithiated phase of $Li_2Ni_2(MoO_4)_3$ has been discovered with a discharge capacity of ≈ 115 mAh $g^{-1}$ (Probaharams *et al*., 2004). The compounds $Li_2M_2(MoO_4)_3$ and $Li_3M(MoO_4)_3$ (M = Fe, Co, Ni) are isostructural and attracted recent attention because they have the ability for reversible Li insertion. This two lithiated compound crystallises in a lyonsite-type structure, which was first described for the Na, Co-containing molybdate with $NaCo_{2.31}(MoO_4)_3$ stoichiometry (Jared *et al*., 2006).

### 2.3.5 $Li_{0.5}Al_{0.5}Mg_2(MoO_4)_3$

$Li_{0.5}Al_{0.5}Mg_2(MoO_4)_3$ is a new molybdenum oxide crystal, its asymmetric unit composed of two $MgO_6$ octahedra and three $MoO_4$ tetrahedra sharing corners as well as (Li/Al) sites (Ennajeh *et al.,* 2013). This compound is composed of infinite chains expanding parallel. A more comparison of the structure of the compound $Li_{0.5}Al_{0.5}Mg_2(MoO_4)_3$ with the $Li_2M_2(MoO_4)_3$ family ($M$ = Mg, Mn, Co, Ni, Cu, Zn) (Efremov & Trunov, 1972; Ozima & Zoltai., 1976) it shows that the swapping to lithium ions from aluminium has modified the crystal structure.

### 2.3.6 $Na_2Fe_2(SO_4)_3$

Low specific capacity is the key issue obstructing wider application of cathode material in the Na-ion battery because of slow ion diffusion and low energy density (Mingzhe *et al*., 2018). Freeze-drying method is used to fabricate $Na_2Fe_2(SO_4)_3$. Synthesised cathode materials can deliver a 3.8 V plateau with discharge capacity of 107.9 Ah at 0.1 C (1 C = 120 Ah) retention capacity above 90% can be offered at a discharge rate of 0.2 C after 300 cycles (Zheng *et al*., 2012).

$NaFe_xCr_{1-x}(SO_4)_2$ (x = 0, 0.8 and 1.0) cathode material for sodium ion batteries has been synthesised by Umair *et al*. (2018). This material was synthesised by sol-gel method by reacting the stoichiometric amounts of reactants. Structural analysis confirmed the formation of a crystalline pure phase adopting a monoclinic crystal structure. $NaFeO_8Cr_{0.2}(SO_4)_2$ had a better thermal stability compared to $NaFe(SO_4)_2$ and $NaCr(SO_4)_2$ . Charge / discharge analysis indicated that the intercalation / de-intercalation of a sodium ion ($Na^+$) into / from $NaFe(SO_4)_2$ ensues at about 3.2 V due to the $Fe^{2+}/Fe^{3+}$ active redox couple (Mingzhe *et al*., 2018).

$Na_{2.5}Fe_{1.75}(SO_4)_3$ exhibited good transport properties with low charge transport activation energy (Plew *et al*., 2019). Electrochemical studies showed improved performance of $Na_{2.5}Fe_{1.75}(SO_4)_3$ compared to $Na_{2+2y}Fe_{2-y}(SO_4)_3$ (Goni *et al*., 2017). A Flux method was used to prepare $NaMgFe(MoO_4)_3$. This compound is isostructural with α-$NaFe_2(MoO_4)_3$ and crystallises in the triclinic space group *P* - 1.

### 2.3.7 $Li_3Fe(MoO_4)_3$

The compounds $Li_3Fe(MoO_4)_3$ and $Li_2Fe_2(MoO_4)_3$ are already known. The related crystal structures have been determined by Klevtsova and Magarill (1970). The structural similarities to $NaCo_{2.31}(MoO_4)_3$ and other framework oxides were noted. These compounds include $Li_3M^{3+}(MoO_4)_3$ (M = Al, Cr, Ga, Sc, In, Co ) (Klevtsov, 1970; Kolitsch and Tillmanns, 2003) and $Li_2M^{4+}(MoO_4)_3$ (M = Ti, Zr, Hf) (Klevtsov and Zolotova, 1973; Klevtsova *et al.*, 1979). $Na_2Fe_2(MoO_4)_3$ has been synthesised by the flux method but not yet successfully synthesized by the sol-gel method and it has only been doped with nickel and zinc only.

### 2.4 Solid electrolyte interphase (SEI) in sodium-ion batteries

Because of the scarcity of lithium-ion batteries in use today, as well as the growing demand for high-density energy storage, researchers are looking for new alternatives to the high-cost lithium-ion battery (Soto *et al.*, 2018). Sodium-ion batteries are a less expensive and more environmentally friendly alternative to lithium-ion batteries. Despite significant research advances in developing electrode materials with high charge storage capacities and rate capabilities, the success of sodium-ion batteries is hampered by the unstable formation of solid electrolyte interphase (SEI) (Martinez *et al.*, 2015). SEI formation has been discussed in the context of lithium-ion systems, but it is still poorly understood in the context of sodium batteries (Soto *et al.*, 2015) (Bommier and Ji, 2018), owing to significant differences between sodium and lithium, such as increased sodium reactivity and increased solubility of degradation products. This means that the knowledge gained from lithium research cannot be directly transferred to sodium research (Mogensen *et al.*, 2015).

#### 2.4.1 The meaning of SEI and its importance

"The solid-electrolyte interphase is a layer that forms at the anode surface for all alkali metal ion batteries that utilize liquid electrolyte" (Bommier and Ji., 2018). Sodium ions are transferred from the cathode cation to and from the anode during charging, and from the anode to the cathode during discharge. As the battery operates and cycles, a solid layer forms at the interphase between the electrolyte and the electrode. The layer formed by the build-up material is known as the Solid-electrolyte interphase (SEI), and it is composed primarily of electrolyte decomposition products (Martinez *et al.*, 2015) (Bommier and Ji., 2018).

The SEI is critical to the battery's operation because it allow the transfer of sodium ions from the electrolytes and it protect the anode by inhibiting the transfer of electrons (Large.stanford.edu). The ideal SEI is thus both an ionic conductor and an electrical insulator, with a thickness that allows ions but not electrons to pass through.

#### 2.4.2 Overcharge protection

The Na dendrite grows at the anode surface, causing the cathode structure to collapse, resulting in a series of reactions that generate heat and gas, eventually leading to a disastrous thermal runaway (Feng *et al.*,2010).

One of the most widely used strategies for building safer SIB is to avoid electrolyte burning, for example, by using non-flammable organic electrolytes. This approach can improve safety performance by reducing or eliminating electrolyte burning at the expense of battery performance. The technique demonstrates the significance of utilizing an inherent and reversible SIB protection technique that is activated before damage occurs under abusive conditions (Kong *et al*., 2019). Overcharge protection is frequently introduced by using (TAC) a shuttle molecule for SIB overcharge protection (Feng et al., 2010)

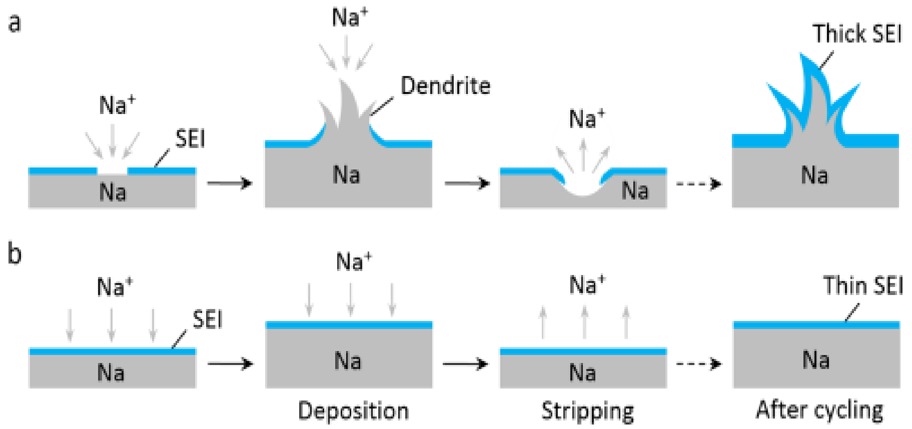

Figure 2.7: Schematic diagram of (a) anode collapsing, (b) prevention of dendrite formation (Jie *et al*., 2015)

Redox shutters are a type of electroactive molecule that can be used as an electrolyte additive to provide reversible overcharge protection. A redox shuttle is oxidized by overcharging, leading to the formation of corresponding radical cations at the cation surface (Sun *et al*., 2019). The resulting positively charged radicals then diffuse to the anode surface where they are reduced. By continuously oscillating between the cathode and the anode, the cell voltage can then be fixed at the reversed redox potential of the oscillating molecule until the end of overcharging. This voltage then protects all cell components from potential damage. Redox shuttles such as 1,4-di-tert-butyl-2-5-dimethoxybenzene (DDB), phenothiazine), Triphenylamine (TPA) etc. and their derivatives have been successfully developed in the past decades (Chen *et al*., 2009).

LIBs have created a large number of '1 redox shuttles, but this does not guarantee that they will work for SIBs, so new redox shuttles may be required. A robust redox shuttle should, ideally, provide effective protection at high overcharge currents with low concentrations (0.1M or wt %). Overcharging is more likely to occur at the end of a fast-charging process of a battery, so a low concentration of additive should be used to maintain battery energy density while maintaining low cell impedance. High compatibility with SIB materials and high mobility or diffusivity are the requirements of molecules that typically have high stability throughout the entire process. This requirement may explain why only few redox shuttles have been developed. The cyclopropenium cation is the smallest aromatic cation and an example of a high chemical stability two-electron buckle system. The trisaminocyclopropenium ion (TAC) is a stable cation that is resistant to hydrolysis and can be converted to stable dications via single-electron oxidation. It was also shown that TAC-based compounds can act as a catholyte in organic redox flow batteries, providing a new platform for SIB overcharge protection. A trisaminocyclopropenium perchlorate ($TAC.ClO_4$) derivative has been identified as a redox shuttle molecule for SIB overcharge protection (Jie., *et al.,* 2020).

### 2.4.3 Toxicity of SIBs

Rechargeable batteries rely heavily on nonrenewable materials and generate massive amounts of end-of-life waste, raising concerns about sustainability in terms of industrial, environmental, and environmental costs. As a result, with naturally available resources and recyclable battery technology, the recyclability and long-term viability of a battery should be considered during the design phase. Using $Na_3V_2(PO_4)_3$ as an electrode material and aluminium foil as the shared current collector, a totally recyclable rechargeable sodium-ion battery with bipolar electrode configuration has been constructed. This design allows for remarkable sodium-ion battery performance in terms of high power output and long-term stability, as well as the 100% recycling of $Na_3V_2(PO_4)_3$ and 99.1% elemental aluminium without harmful wastes, resulting in a solid-component recycling efficiency of >98.0%. The successful integration of sustainability into battery design points to next-generation energy storage technologies that will be able to achieve closed-loop recycling and reutilization of battery components.

## 2.5 Literature synthesis methods

$Fe(MoO_4)_3$ has been synthesised by solid-state precipitation by Shiliang *et al,* 2010. Peng *et al*., (2010) also synthesised $Fe_2(MoO_4)_3$ by the precipitation method. A $Na_2Fe_2(MoO_4)_3$ powder has been synthesised using a technique of soft combustion at low temperature, namely, the glycine nitrate method. $Na_2Fe_2(MoO_4)_3$ composites have been prepared by simple hand grinding using a mortar and pestle (Atin *et al*, 2016). $Na_2Fe_2(MoO_4)_3$ was also synthesised by a sol-gel process using stoichiometric ratios ( Umair *et al*., 2018).

In this study, the sol-gel method is used because it is inexpensive, easy and its product are pure and in high yield, very fine particles that are more homogenous in terms of size and shape (Patil *et al*., 2002)

# Chapter 3: Research methodology

## 3.1 General experimental conditions

Table 3.1: Chemicals used

| List of chemicals | Chemical formula | Purity of material,% | Molar mass g/mol |
|---|---|---|---|
| Sodium nitrate | $Na_2NO_3.H_2O$ | 99.0 | 241.86 |
| Iron(II) nitrate | $Fe_2(NO_3)_2.6H_2O$ | 97.0 | 179.86 |
| Zinc nitrate | $Zn(NO_3)_2$ | 98.0 | 189.36 |
| Copper dinitrate | $Cu(NO_2)_3$ | 98.0 | 187.56 |
| Potassium chloride | KCl | 99.0 | 74.55 |
| Chromium(III) nitrate | $Cr(NO_3)_3$ | 99.9 | 238.01 |
| Citric acid | $C_6H_8O_7$ | 99.0 | 210.14 |
| Calcium carbonate | $CaCO_3$ | 98.0 | 100.08 |
| Molybdenum(IV)oxide | $MoO_2$ | 97 | 127.94 |

All material were purchased from Sigma Aldrich. The materials were used without further purification.

## 3.2. Experimental

$Na_2Fe_2(MoO_4)_3$ was synthesised by a sol-gel process using sodium nitrate, iron nitrate monohydrate and ammonium molybdate in stoichiometric ratios ( Umair *et al*., 2018). All the precursors were dissolved in 100 ml distilled water with continuous stirring maintaining the temperature at 80 °C. The solution was stirred at a constant temperature to evaporate until the gel was formed. The resulting solution was dried at 120 °C in an oven for 6 hours. After cooling in the oven the gel was ground homogeneously into a fine crystalline powder and then calcined at 600 °C for 3 hours in the air to obtain pure $Na_2Fe_2(MoO_4)_3$ ( Umair *et al*., 2018).

### Experimental procedure for doping

$Na_2Fe_{2-x}M_x(MoO_4)_3$ was synthesised similarly using sodium nitrate, iron nitrate monohydrate and ammonium molybdate in stoichiometric ratios ( Umair *et al*., 2018. All the precursors were dissolved in 100 ml distilled water with continuous stirring maintaining the temperature at 80 °C. When doping with copper at X= 0.1 the copper nitrate was added after all the other reactant are dissolved. The solution was stirred at a constant temperature to evaporate until the gel was formed. The resulting gel was dried at 120 °C in an oven for 6 hours. This process was repeated with all doping at different concentrations (X = 0. 1 – 0.5) and doping with different materials at the iron and sodium sites. After cooling in the oven the gel was homogeneously ground homogeneously into a fine crystalline powder and then calcined at 600 °C for 3 hours in the air to form pure $Na_2Fe_{2-x}M_x(MoO_4)_3$ ( Umair *et al*., 2018).

## 3.3. Instrumental analysis

Calcinated samples were analysed to confirm the formation and the presence of the structure. A Fourier transform infrared spectroscopy was used to characterise the bond structure of all the synthesised samples. X-ray diffraction analysis was be used to confirm the crystallinity of the structures and atomic spacing. Scanning electron microscopy-energy-dispersive spectroscopy (SEM-EDS) will be used for qualitative elemental analysis and morphology of the materials. Raman spectroscopy (Raman) was used to determine the chemical structure, phase and polymorphy, crystallinity and molecular interactions. Fourier transform infrared spectroscopy (FTIR) was used to confirm the presence of metal oxide vibrational frequencies.

### 3.3.1. Fourier transform infrared spectroscopy (FTIR)

An Alpha FTIR spectrometer (Bruker Optics 7.0) equipped with alpha platinum was used to characterise the bonds of all the synthesised samples. Parameters include a resolution of 4 $cm^{-1}$, sample and background scan time of 24 scans. All the samples were being analysed at 20 °C (Ball, 2006). The presence of metal oxide vibrational frequencies of the expected spinel structure would be observedif they are successfully synthesized (Bassler *et al.,* 1981)

### 3.3.2. X-ray diffraction spectroscopy (XRD)

X-ray diffraction spectroscopy is a non-destructive technique for analysing a material's crystal structures and atomic spacing. X-rays are used to make contact with the synthesised specimen at various angles, and the diffraction intensities are measured for each. Every chemical compounds crystalline structure has a distinct diffraction pattern. The International Center for Diffraction Data (ICDD) keeps track of all known diffraction patterns in a database. To identify the substance, these known patterns can be compared to an unknown specimen. (Dutrow and Clark, 2011). The crystalline phases of all the synthesised samples were identified by XRD spectrometry using Cu K α radiation ($\lambda = 1.5408$) at ambient temperature. The XRD measurements were collected from 5° to 80° ($2\Theta$) and used to investigate the crystal structure of the materials. XRD can also be used for quality control. The crystallite size can be calculated using the Debye-Scherrer method.

**Calculating the crystallite size**

The average crystallite size was calculated from the XRD pattern according to the line width of the (111) plane reflection peak using the Scherrer equation:

$$\mathrm{Dp} = \frac{0.94\lambda}{\beta \cos\Theta} \qquad \dots (1)$$

Where $D_p$ is the average crystallite size in nm

$\beta$ is the line broadening at half the maximum intensity in radians

$\Theta$ is the Bragg's angle in degrees

$\lambda$ is the x-ray wavelength (0.15406 nm)

The particle size was calculated in nm for each sample

### 3.3.3. Scanning electron microscopy-energy-dispersive spectroscopy (SEM-EDS)

The qualitative elemental analysis and morphology of the materials were characterised by SEM-EDS at ambient temperature. The SEM-EDS used was a Tescan Mira 3 FEG-SEM (Field emission scanning electron microscope) and is a recognized technique for the qualitative elemental analysis of materials. The SEM features a high brightness Schottky emitter allowing users to generate high resolution micrographs down to 1 nm. It is built around the large XMU chamber, which can analyse as large as 300 mm wide area/sample size. The Peltier stage allows investigation of sample behaviour at temperatures between -70 and 50 ºC. The SEM-EDS measurements were collected from 0 to 20 keV and provided information on the homogeneity, element distribution and changes in composition.

### 3.3.4 Raman spectroscopy

“Raman spectroscopy is a non-destructive chemical analysis technique that provides detailed information about chemical structure, phase and polymorphism, crystallinity, and molecular interactions” (www.slideshare.net). When light interacts with molecules in the liquid, gas, or solid state, the vast majority of protons are scattered or dispersed with the same energy as the incident photons. This is called elastic scattering. When photons interact with molecules, the molecule can be promoted to a higher energy state, or one of several outcomes can occur. Such a result would be that the molecule relaxes to a different vibrational energy level than its initial state, resulting in a photon with a different energy. The Raman shift is the difference between the energy of the incident photon and the energy of the scattered photon. In this work, a witec Raman optical microscope, was used to record the Raman spectra of the samples in the wavenumber region of interest 10 - 1500 $cm^{-1}$. The samples were placed on the microscopic glass substrate and placed under the 100x Nikon objective and focused. The measurement was recorded at 2 milliwatt (mW) using the 532 nm laser at 30s integration time and 4 accumulations.

### 3.3.5 X-ray fluorescence spectroscopy

The elemental composition of materials can be determined using XRF, a non-destructive analytical method. XRF analysers determine the chemistry of a compound by measuring the fluorescent x-ray emitted by a sample when excited by a primary x-ray source. Each element in a sample emits a distinct set of fluorescent x-rays that are unique to that element, which is why XRF spectroscopy is an ideal technology for qualitative material composition analysis. S1 Titan model 800 and 500s alloy testers, Graphene window sdd, 20mm active area, typical resolution,50 KV x-ray tube is the XRD equipment that was used to characterise the products.

# Chapter 4: Results and Discussion

This chapter discusses the characterisation results for $Na_2Fe_2(MoO_4)_3$ and its doped compounds.

## 4.1 X-ray diffraction

XRD studies of the prepared samples showed the formation of the crystalline spinel phase. Figure 4.1 shows the x-ray diffraction patterns of $Na_2Fe_2(MoO_4)_3$ and its doped materials. The synthesized samples showed both crystalline and amorphous phases. From Table 4.1, well-defined x-ray diffraction patterns or peaks indicate the crystalline nature of all the samples. The XRD patterns of the $Na_2Fe_2(MoO_4)_3$ and its doped forms present nine characteristic peaks at 13.87°, 22.05°, 25.60°, 29.15°, 34.64° and 55.62° 2 theta that corresponds to crystal planes of (200), (311), (212), (124), (420) and (0.108) (Dudney *et al.*, 1999). However, the samples was not fully crystalline as the peaks were not sharp. There was an increase in crystallinity as the dopant concentration was increased. In single doping with copper at X = 0.1 Figure 4.1(a) atom equivalent and X = 0.4 the peaks become more intense and narrower hence more crystalline. Doping with X = 0.2 show the Flattering of peaks, which might be due to high doping which can cause inconsistent results, doping with purity of 97% might also be part of drawback of this fluctuation of the crystallinity. This figure shows XRD patterns doped with copper at concentration 0.1, 02 and 0.4 as the concentration cu increases from 0.1 to 0.2 the peaks gradually shift to the left and the angle decreases. According to the Bragg equation when the distance increases with the decreasing angle. The reason for this might be that as the concentration of Cu goes up more copper ions was incorporated into the $Na_2Fe_2(MoO_4)_3$ lattice. The increase of copper more leads to growth of lattice strain that prevent the further enhancement of crystallization, at high concentration of 0.4 a considerable amount secondary phase appears due to the collapse of the lattice. This drawback was also witnessed with Raman spectra that shows the more crystal peaks at 0.2 concentration where the doping affected the peaks with broadening and peak shifting.

From Figure 4.1(b), it can be seen that the prepared materials are fully crystalline, as the ratio of zinc increases to 0.3 the peaks become sharp and the doped material become more crystalline than the parent structure. However increasing x to 0.4 the peaks become less crystalline, as the high dopant amount destroy the crystalline structure of the parent structure, as only a few peaks were detected. Prominent peaks appearing at 2θ ~ 50 are the expected peaks from the parent structure, which shows that there was still crystallinity after doping and the peaks where affected differently by doping vibration mode. Doping with calcium in the sodium sites (Figure 4.1(c), showed that the peaks become sharper and the structure become more crystalline than the parent structure. Doping with calcium at 0.1 shows very sharp peaks and thus high crystallinity compared to other dopants but increasing the concentration of calcium to 0.2 no peak was detected.

Doping with chromium (Figure 4.1(d)) on the sodium sites, the sizes of the peaks increase with an increase in Cr ratio and the peaks become sharper. This showed that doping can increase the crystallinity of the material. When x = 0.4 the material lost its crystallinity as the detected peaks become flat. From Figure 4.1(e) doping with potassium doesn't improve the crystallization of the parent structure.

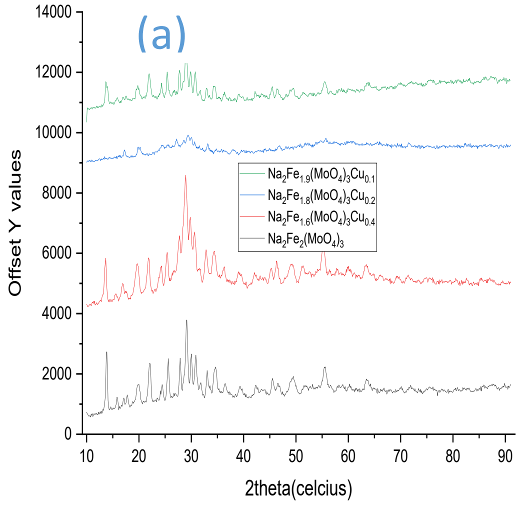

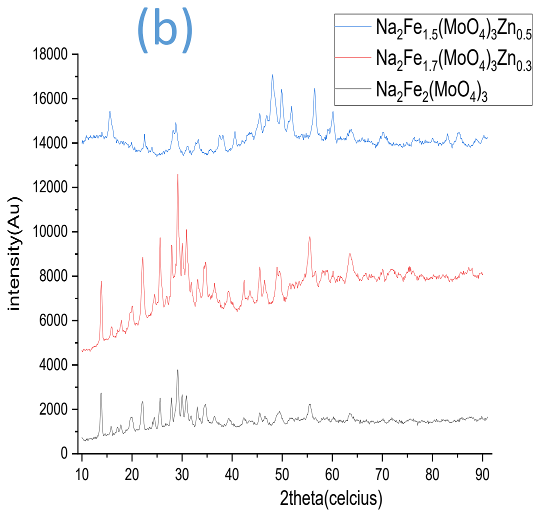

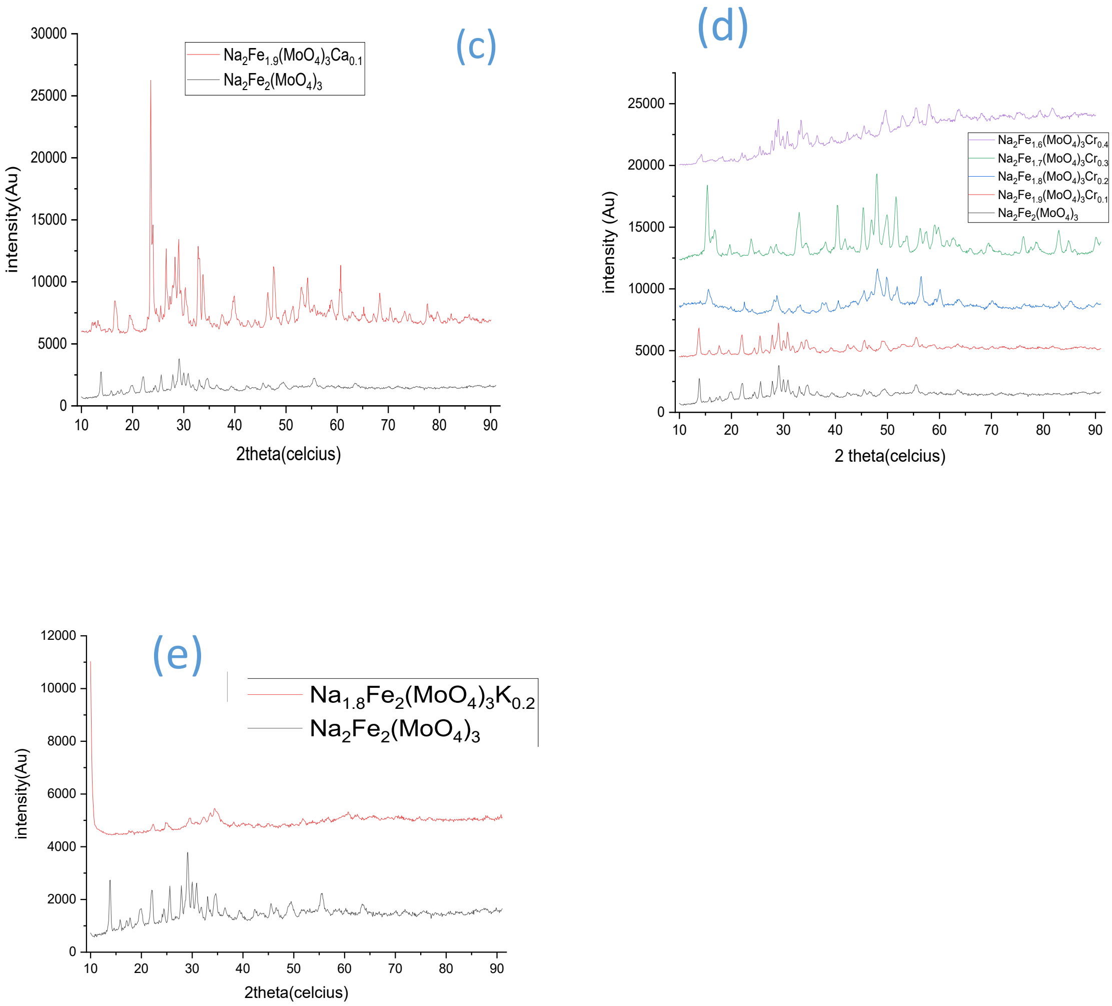

-

**Figure 4.1:** XRD patterns of $Na_2Fe_2(MoO_4)_3$ parent structure doped with different concentration (a) $Na_2Fe_2(MoO_4)_3$ doped with copper,(b) $Na_2Fe_2(MoO_4)_3$ doped with zinc,(c) $Na_2Fe_2(MoO_4)_3$ doped with calcium and (e) $Na_2Fe_2(MoO_4)_3$ doped with potassium.

The width of a peak varies inversely with crystallite size and as the crystallite size gets smaller the peaks get broader. As seen in Table 4.1 the crystallites of the parent material were smaller than those of the doped metal complexes as the dopant concentration increased the crystallite size increased and therefore the material became amorphous and showed less crystallite. The broadening of the peaks might be due to strain and composition in homogeneities.

**Table 4.1**: Crystallite sizes of $Na_2Fe_2(MoO_4)_3$ doped with copper

| **Samples** | **Crystallite size (nm)** |
|---|---|
| (a) $Na_2Fe_2(MoO_4)_3$ | **14.49** |
| (b) $Na_2Fe_{1.9}(MoO_4)_3Cu_{0.1}$ | **20.10** |
| (c ) $Na_2Fe_{1.8}(MoO_4)_3Cu_{0.2}$ | **24.90** |

| | |
|---|---|
| (d) $Na_2Fe_{1.6}(MoO_4)_3Cu_{0.4}$ | **19.22** |

**Table 4.2**: crystallite sizes of $Na_2Fe_2(MoO_4)_3$ doped with zinc

| **Samples.** | **Crystallite size (nm).** |
|---|---|
| (e) $Na_2Fe_{1.7}(MoO_4)_3Zn_{0.3}$ | **23.99** |
| (f) $Na_2Fe_{1.5}(MoO_4)_3Zn_{0.5}$ | **30.01** |

**Table 4.3:** Crystallite size of $Na_2Fe_2(MoO_4)_3$ doped with calcium

| **Samples.** | **Crystallite size (nm).** |
|---|---|
| **(g)** $Na_2Fe_{1.9}(MoO_4)_3Ca_{0.1}$ | **15.06** |

**Table 4.4** Crystallite sizes of $Na_2Fe_2(MoO_4)_3$ doped with chromium

| **Samples.** | **Crystallite size (nm).** |
|---|---|
| (h) $Na_2Fe_{1.9}(MoO_4)_3Cr_{0.1}$ | **41.08** |
| (i) $Na_2Fe_{1.8}(MoO_4)_3Cr_{0.2}$ | **24.40** |
| (j) $Na_2Fe_{1.7}(MoO_4)_3Cr_{0.3}$ | **27.94** |
| (k) $Na_2Fe_{1.6}(MoO_4)_3Cr_{0.4}$ | **20.04** |

**Table 4.5**: crystallite sizes of $Na_2Fe_2(MoO_4)_3$ doped with potassium.

| **Samples.** | **Crystallite size (nm).** |
|---|---|
| (l) $Na_2Fe_2(MoO_4)_3$ | **14.49** |
| (m) $Na_{1.8}Fe_2(MoO_4)_3K_{0.02}$ | **14.10** |

## 4.2 Raman spectroscopy

Raman spectroscopy is more sensitive in distinguishing types of crystal symmetries whose atomic arrangements were closely related. As shown in Figure 4.2, Raman spectra of the Na ion $Fe_2(MoO_4)_3$ were collected to see if evidence of the perturbation could be uncovered. Raman spectroscopy showed that the $Fe_2(MoO_4)_3$ had monoclinic structural bands at 988, 967, and 930 $cm^{-1}$ (symmetric stretches of the terminal Mo=O bonds in three different $MoO_4$

tetrahedra); 817, 776 c m$^{-1}$ (asymmetric stretches of MoO4 units); and 356 cm$^{-1}$ (asymmetric elongation modes of MoO4 units) (MoO4 bending mode). All Raman bands in the analyzed and doped MoO4 units appear to be faint or unresolved. In the Raman spectrum of pristine material, the strongest asymmetric stretching band of the $MoO_4$ units appears to be very broad and weak in the spectra of samples containing sodium.

The weaker bending and symmetric stretching modes, on the other hand, remained unresolved. Furthermore, there was a shift in the locations of Raman bands. This broadening and loss of intensity could be due to the redistribution of electron density in the Mo-O bonds caused by the intercalation of alkali guest ions into the pristine material, which could also be influenced by the reduction of $Fe^{3+}$ ions to $Fe^{2+}$ (Mhiri *et al.*, 2016).

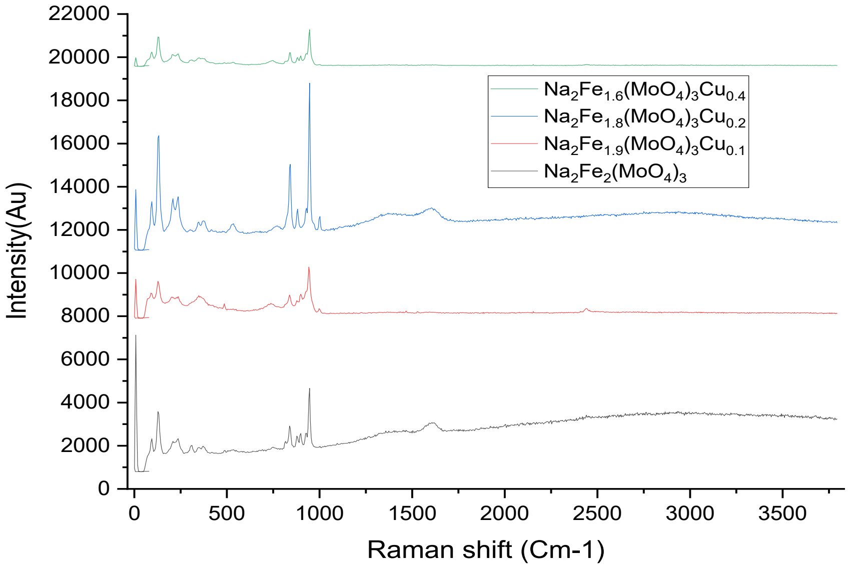

**Figure 4.2** The Raman spectra of copper-doped compounds at varying Cu amounts showing the Raman shift

In the lower energy region from Figure 4.2, less intense Raman peaks can be observed. Raman modes was observed for sodium iron molybdate at around 250 and 356 cm$^{-1}$. In the 500 - 750 cm$^{-1}$ region, no Raman peaks were present. These signals was most likely due to the coupling between some of the vibrations. From the Raman spectra, it can be seen that doping of parent structure does not introduce new intense Raman modes, and thus no impurity phases can be detected.

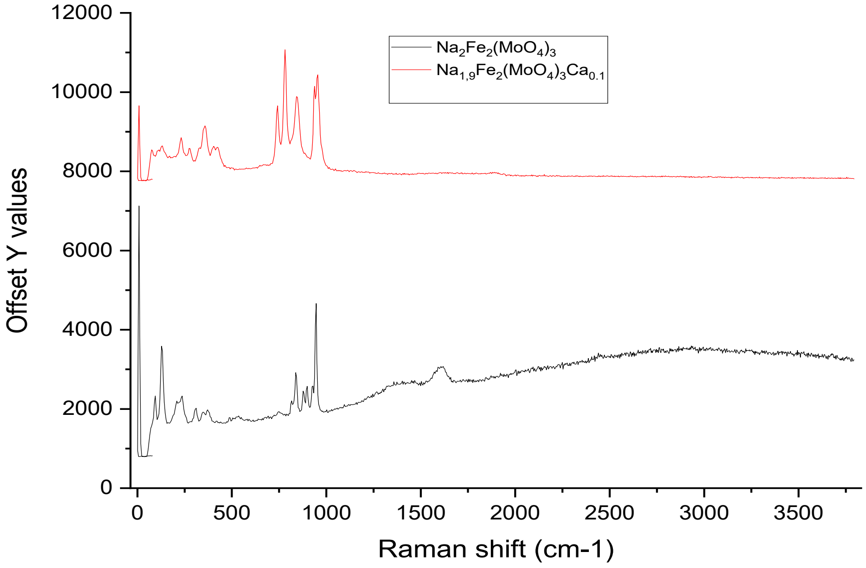

**Figure 4.3:** The Raman spectra of calcium-doped compounds at varying Ca amounts showing the Raman shift of doped cathode material

Figure 4.4 shows the Raman spectra of parent structure doped with different amounts of dopant range, material synthesized by sol-gel method at 600 °C for 3 hours. Raman spectroscopy revealed that the $Na_2Fe_2(MoO_4)_3$ had monoclinic structure bands 988, 967, and 930 $cm^{-1}$ symmetric stretching modes of terminal Mo = O bonds in three distinct $MoO_4$ tetrahedra; 817, 776 $cm^{-1}$ asymmetric stretching modes of $MoO_4$ units; and 356 $cm^{-1}$ asymmetric stretching modes of $MoO_4$ units. Well-defined Raman modes were observed for undoped and doped structures in the lower energy part of the spectra, that was, around 250 - 500 $cm^{-1}$. In the 500 - 750 $cm^{-1}$ region, there was no Raman structures that were present. From 111 $cm^{-1}$ of the Raman spectra, it can be seen that doping of $Na_2Fe_2(MoO_4)_3$ does not introduce new intense Raman modes, and thus no impurity phases can be detected.

It can be seen from the spectra below that increasing the concentration of chromium destroy the crystallinity of the $Na_2Fe_2(MoO_4)_3$ and then some peaks wasn't visible in the Raman spectra when Cr = 0.3 and 0.4. Not all the bands are affected equally by the presence of the heterogeneity in the crystal. Those Raman bands that arise after doping with 0.2 concentration that was not detected on 0.1 arise from the lattice vibration modes that involve a significant contribution of atomic motion from the substituted atom was manifesting significant broadening and shifting of peak position. The saturation of the lattice can also cause peak shifting and broadening.

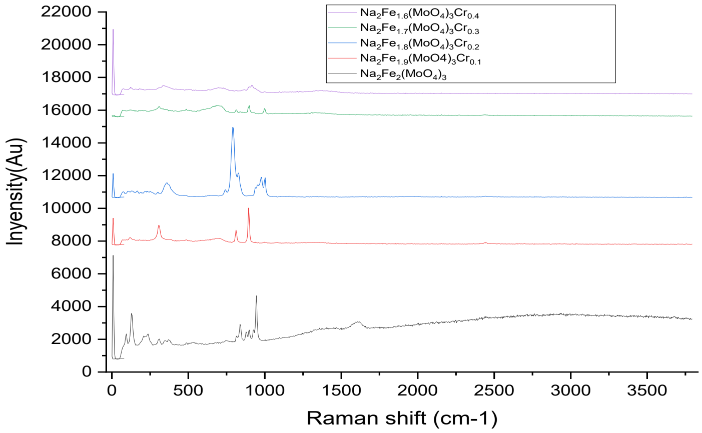

**Figure 4.4** The Raman spectra of chromium-doped compounds at varying chromium amounts showing the Raman shift between the doped cathode materials.

Figure 4.5 shows the Raman spectra of parent structure doped with different amounts of dopant range, material synthesized by sol-gel method at 600 °C for 3 hours. Raman spectroscopy revealed that the $Na_2Fe_2(MoO_4)_3$ had monoclinic structure bands 988, 967, and 930 $cm^{-1}$ symmetric stretching modes of terminal Mo = O bonds in three distinct $MoO_4$ tetrahedra; 817, 776 $cm^{-1}$ asymmetric stretching modes of $MoO_4$ units; and 356 $cm^{-1}$ asymmetric stretching modes of $MoO_4$ units. Well-defined Raman modes were observed for undoped and doped structures in the lower energy part of the spectra, that was, around 250 - 500 $cm^{-1}$. In the 500 - 750 $cm^{-1}$ region. There were no Raman structures that were present. From the Raman spectra, it can be seen that doping of $Na_2Fe_2(MoO_4)_3$ does not introduce new intense Raman modes, a vibration stretch and thus no impurity phases can be detected. It can be seen from the spectra below that increasing the concentration of zinc destroy the crystallinity of the $Na_2Fe_2(MoO_4)_3$ and then some peaks aren't visible in the Raman spectra when Zn = 0.5. Those Raman bands that arise after doping with 0.3 concentration that was not detected on parent structure arise from band broadening and shifting since those peaks where clustered together, the bands of Raman was not affected equally by doping on the lattice. The saturation of the lattice can also cause peak shifting and broadening.

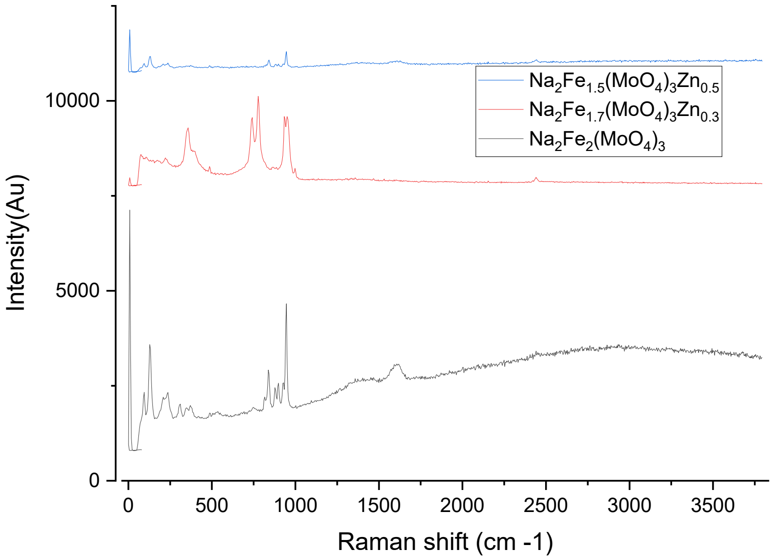

**Figure 4.5** The Raman spectra of the parent structure doped with different amounts of K dopant range amounts showing the Raman shift between the doped cathode materials

Figure 4.6 shows the Raman spectra of parent structure doped with different amounts of dopant material synthesized by sol-gel method at 600 °C for 3 hours. Raman spectroscopy revealed that the $Na_2Fe_2(MoO_4)_3$ had monoclinic structure bands 988, 967, and 930 $cm^{-1}$ symmetric stretching modes of terminal Mo = O bonds in three distinct $MoO_4$ tetrahedra; 817, 776 $cm^{-1}$ asymmetric stretching modes of $MoO_4$ units; and 356 $cm^{-1}$ asymmetric stretching modes of $MoO_4$ units. Well-defined Raman modes was observed for undoped and doped structures in the lower energy part of the spectra, that was, around 250 - 500 $cm^{-1}$. In the 500 - 750 $cm^{-1}$ region, there was no Raman structures that were present. From the Raman spectra, it can be seen that doping of $Na_2Fe_2(MoO_4)_3$ does not introduce new intense Raman modes, and a vibration stretch and thus no impurity phases can be detected. It can be seen from the spectra below that increasing the concentration of potassium destroy the crys tallinity of the $Na_2Fe_2(MoO_4)_3$ and then some peaks aren't visible in the Raman spectra when potassium concentration is 0.2.

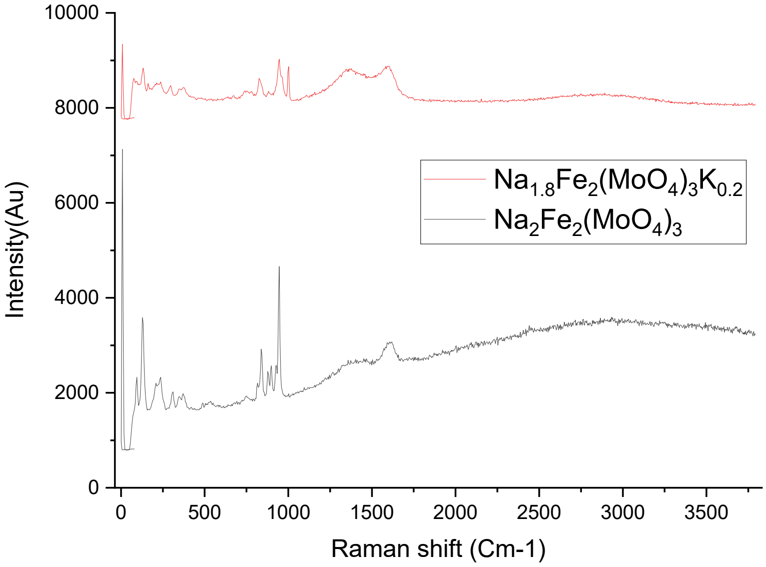

**Figure 4.6** The Raman spectrum of potassium-doped compounds at varying K amounts, showing the Raman shift between the doped cathode materials

## 4.4 Scanning electron microscopy (SEM)

The morphologies of $Na_2Fe_2(MoO_4)_3$ and those of doped materials were shown in Figures 4.7 to 4.12. A heterogeneous morphology of samples indicates an agglomerated grain structure. It can be observed the samples were less agglomerated (small particles) which suggests that the prepared samples have better electrochemical performance. There was metal complexes that were more agglomerated and form large particles. The twelve synthesized and characterized materials was less crystalline. Furthermore, the synthesized parent structure, $Na_2Fe_2(MoO_4)_3$, was more agglomerated compared to all the synthesized doped samples. The shape of particles of all the twelve samples was irregular.

Figure 4.7(a) shows the morphology aspect of the $Na_2Fe_2(MoO_4)_3$ which was examined using SEM. The SEM micrograph reveals that the morphology consists of a smooth surface with, different particle sizes and few irregular shapes. From the particle size of the demonstrated compound below they were not uniformly distributed in size and the particle size of the compound was approximately 1 µm. It can also be observed that agglomeration takes place among the particles. Figure 4.7(b) the particle size are not uniformly distributed in size and the particle size was approximately 2 µm.

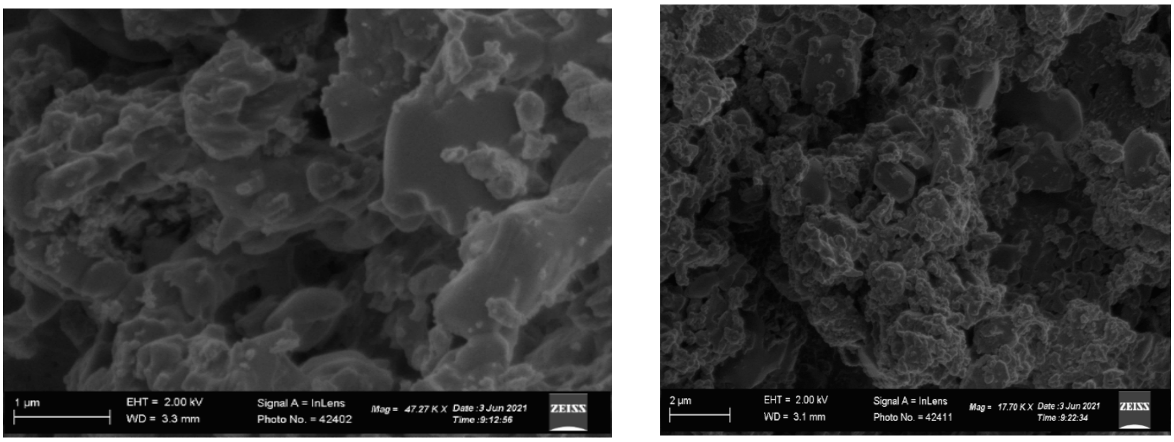

Figure 4.7: SEM micrographs of (a) $Na_2Fe_2(MoO_4)_3$ (b) $Na_2Fe_{1.6}(MoO_4)_3Cu_{0.4}$

Figure 4.8(a) $Na_2Fe_2(MoO_4)_3$ shows the morphological aspect of the doped (b) $Na_2Fe_{1.9}(MoO_4)_3Cu_{0.2}$ which was examined using SEM. The SEM micrograph reveals that the morphology consists of a smooth surface with few irregular shapes. The agglomeration of the samples was less agglomerated and have better electrochemical performance. Figure 4.8(b) have a flat particle shape with a rod. From the particle size of the demonstrated compound below they were not uniformly distributed in size and the particle size of the compound was approximately 1 - 2 µm. It can also be observed that agglomeration takes place among the particles

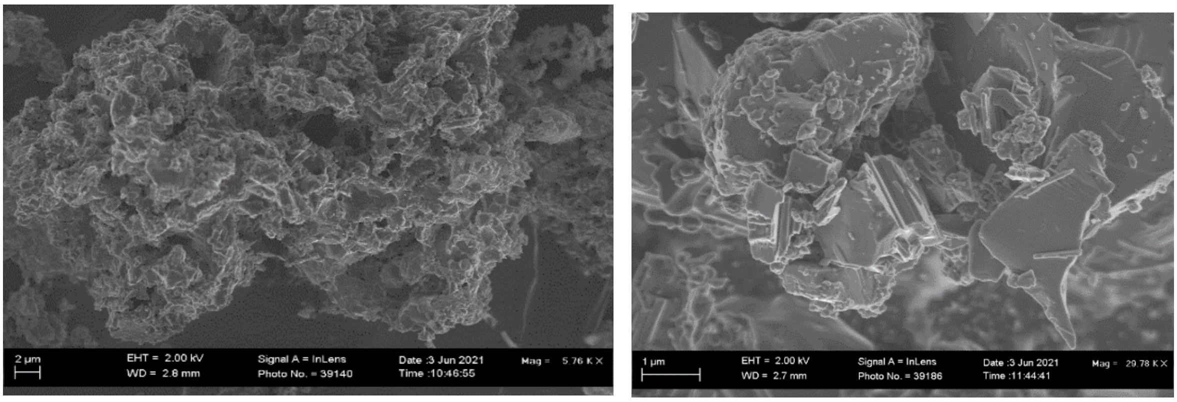

Figure 4.8: SEM micrographs of (a)$Na_2Fe_{1.9}(MoO_4)_3Cu_{0.2}$ (b) $Na_2Fe_{1.9}(MoO_4)_3Cu_{0.1}$

Figure 4.9 shows the morphology of the Zn doped $Na_2Fe_2(MoO_4)_3$ which was examined using SEM. The SEM micrograph reveals that the morphology consists of a smooth surface with few irregular shapes. The agglomeration of the samples were more agglomerated and have better electrochemical performance. Figure 4.9(b) have a rod particle shape. It can be observed that the particle size of the compound was not uniformly distributed in size and the particle size of the compound was approximately 1 µm. It can also be observed that agglomeration takes place among the particles

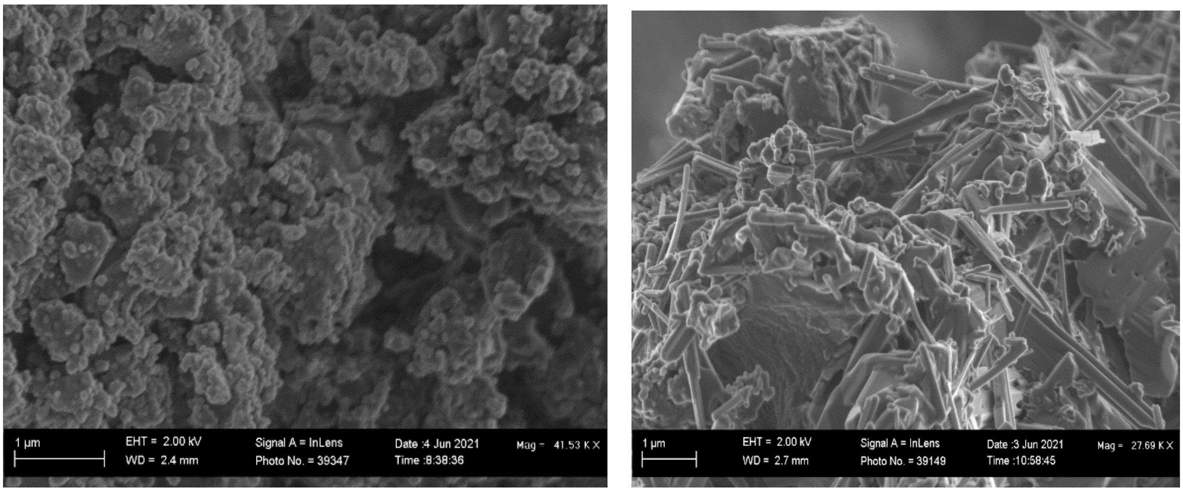

Figure 4.9: SEM micrographs of (a) $Na_2Fe_{1.5}(MoO_4)_3Zn_{0.5}$ (b) $Na_2Fe_{1.7}(MoO_4)_3Zn_{0.3}$

Figure 4.10(a) shows the morphological aspect of the Ca doped $Na_2Fe_2(MoO_4)_3$ which was examined using SEM. The SEM micrograph reveals that the morphology consists of a smooth surface with rod shapes. The agglomeration of the samples was more distinct in the Cr doped $Na_2Fe_2(MoO_4)_3$ as shown in Figure 4.10(b) with an irregular particle shape. It can be observed that the particle size of the compound was not uniformly distributed and were approximately 1 µm. It can also be observed that agglomeration takes place among the particles.

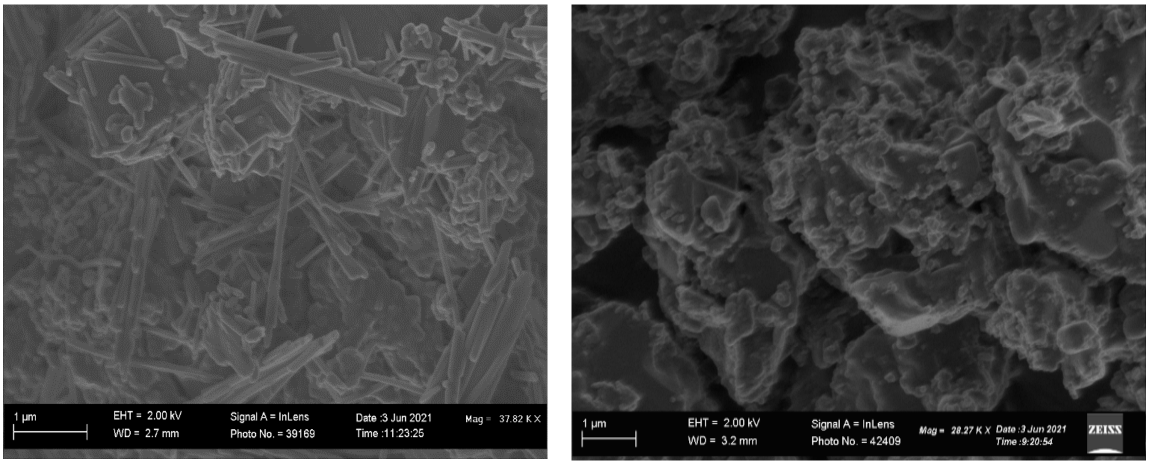

Figure 4.10: SEM micrographs of (a) $Na_{1.9}Fe_2(MoO_4)_3Ca_{0.1}$ (b) $Na_2Fe_{1.9}(MoO_4)_3Cr_{0.1}$

Figure 4.11(b) show the morphology of the Cr doped $Na_2Fe_2(MoO_4)_3$ examined using SEM. The SEM micrograph reveals that the morphology consists of a smooth surface with flaky particle shapes. The sample was less agglomerated and expected to have better electrochemical performance. The electrochemical performance significantly depend on the material with which they are made specifically on the surface area (Karim *et al*, 2019). Figure 4.11(b) have an irregular particle shape. It can be observed that the particle size of the compound was not uniformly distributed approximately 1 µm. It can also be observed that agglomeration takes place among the particles.

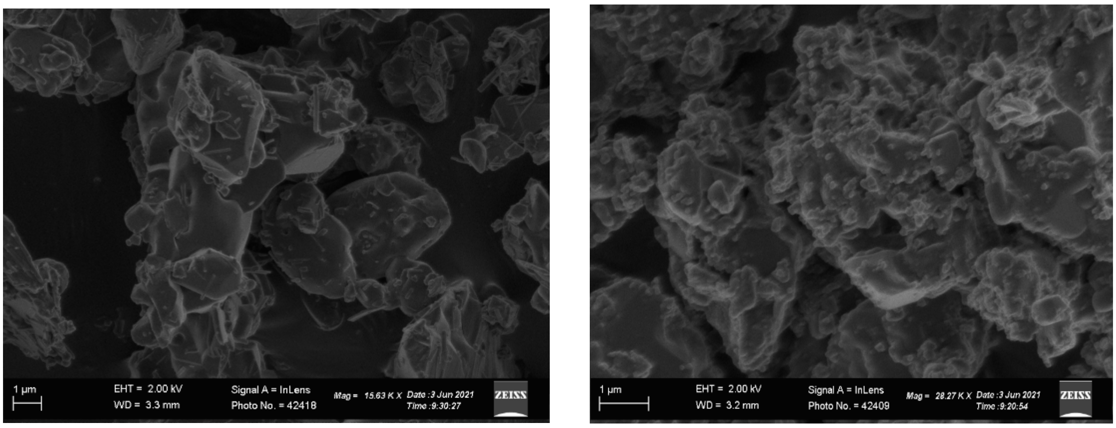

Figure 4.11: SEM micrographs of (a) $Na_2Fe_{1.8}(MoO_4)_3Cr_{0.2}$ (b) $Na_2Fe_{1.7}(MoO_4)_3Cr_{0.3}$

Figure 4.12(a) shows the morphology of the Cr doped $Na_2Fe_2(MoO_4)_3$ which was examined using SEM. The SEM micrographs reveal that the morphology consists of a smooth surface with rod and angular shapes. It can be observed that the particle size of the compound were not uniformly distributed was approximately 1 µm. It can also be observed that agglomeration takes place among the particles. 4.12(b) shows the morphology of K doped $Na_2Fe_2(MoO_4)_3$ The SEM micrographs reveal that the particles consist of smooth surfaces with rod and angular shape. It can be observed that the particle size were not uniformly distributed at approximately 1 µm.

When doping at Fe site the surface have irregular shape and doping at Na site the surface have rod shape. The correlation between the XRD and the particle of SEM, when doping at Na site the surface had rod shape and hence more crystal because not more than 0.1 concentration was needed to increase the crystallinity.

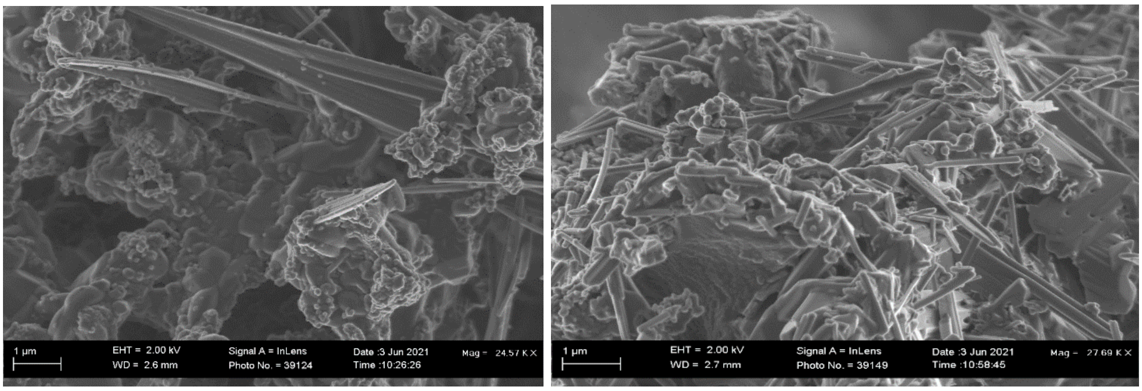

Figure 4.12: SEM micrographs of (a) $Na_2Fe_{1.6}(MoO_4)_3Cr_{0.4}$ (b) $Na_{1.8}Fe_2(MoO_4)_3K_{02}$.

According to Huu *et al* 2021 Figure 4.8(b), 4.9(b), 4.10(a) and 4.12(a & b) the rod like shape is described as the rose-like. This two dimension morphology was thought to expose more interior, which was beneficial for chemical and physical characterisation. This dimension has the unique properties such as high mechanical flexibility, short ion diffusion pathway and large active surface which was expected to provide more advantages for electrochemical reactions and energy storage. The alignment creates open stacking gaps between them, offering a porous structure to facilitate for electrolytes penetration, improve electronic and ionic transport, which accelerates sodium ions kinetics and supply more active sites. This type of cathode provide a specific capacity of 90.2 MAh.g$^{-1}$ after 100 cycles this is due to their well 3D stacking architecture and isotropic nature that can accommodate a large volume change during intercalation /deintercalation of sodium ions.

## 4.4 Energy dispersive X-ray spectroscopy (EDS) (Maphiri , 2017)

The EDS spectra were recorded to identify the chemical composition of the $Na_2Fe_2(MoO_4)_3$ cathode materials, as a weight percentage. To confirm the compositional distribution of the constituent elements of the powder samples, EDS mapping was used and the image of an undoped sample was displayed in Figure 4.1.3. Image of individual elements were displayed below the layered image, and they show that all elements are homogeneously distributed.

As indicated by the spectra in Figure 4.14(a), the presence of the elements sodium, molybdenum, iron and oxygen was confirmed. No other peaks of impurities were detected suggesting that the prepared materials are free of impurities. EDS has the limitation of not detecting very light elements, especially those with an atomic number lower than that of sodium.

Figure 4.14(b) shows the presence of sulphur, which was not desired in $Na_2Fe_{1.9}(MoO_4)_3Cu_{0.1}$.This was due to the Cu starting material used in the synthesis. Therefore this sample was not free of impurities. Images of each elements maps are displayed below the layered image, and they show that all elements are homogeneously distributed.

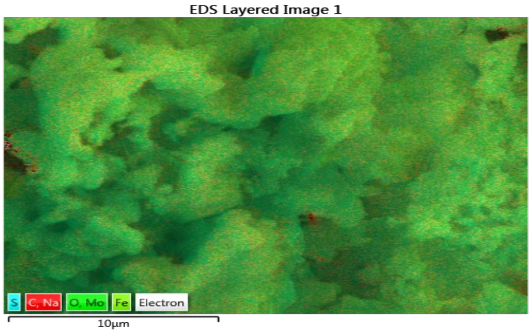

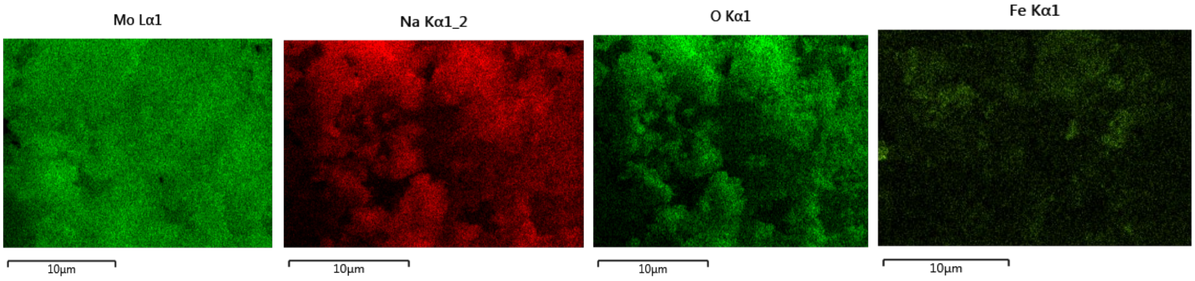

**Figure 4.13:** SEM image with corresponding EDS elemental mappings of $Na_2Fe_2(MoO_4)_3$ annealed at 600 °C for 3 hours

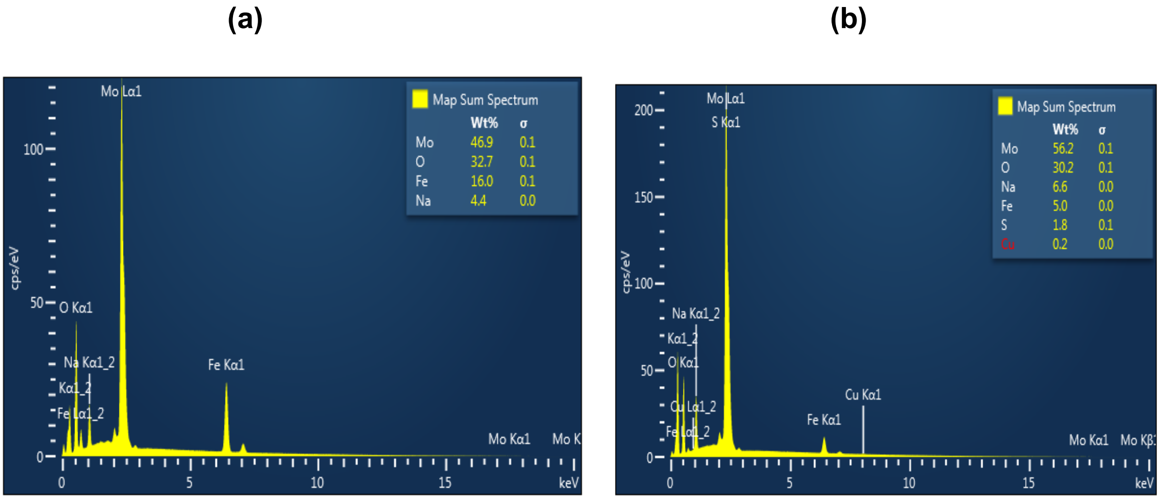
(a) (b)

**Figure 4.14:** EDS spectra of (a) $Na_2Fe_2(MoO_4)_3$ b) $Na_2Fe_{1.9}(MoO_4)_3Cu_{0.1}$

Similarly, Figure 4.15 shows the presence of lead and sulphur impurities. The presence of these elements can be linked to the starting material. The presence of the desired material is also shown

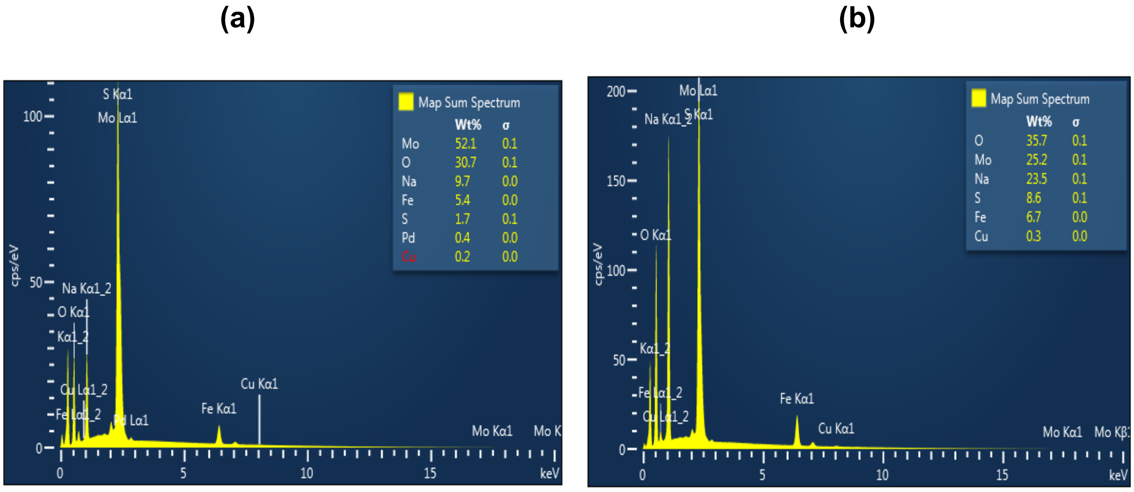
(a) (b)

Figure 4.15: EDS spectra of (a) $Na_2Fe_{1.9}(MoO_4)_3Cu_{0.2}$ (b) $Na_2Fe_{1.9}(MoO_4)_3Cu_{0.1}$

Figure 4.16 shows the presence of zinc, which were introduced as a dopant other impurity peaks were shown, suggesting that the prepared material was not free from impurity.

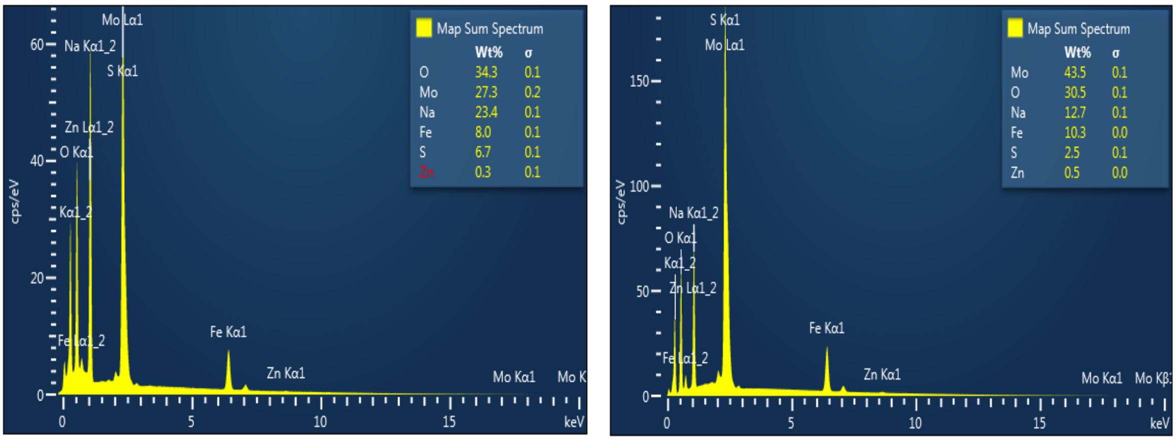

(a) (b)

Figure 4.16: EDS spectra of (a)$Na_2Fe_{1.7}(MoO_4)_3Zn_{0.3}$ (b) $Na_2Fe_{1.5}(MoO_4)_3Zn_{0.5}$

Figure 4.17 shows the presence of calcium and sulphur in $Na_{1.9}Fe_2(MoO_4)_3Ca_{0.1}$, which suggest that the prepared material was not free of impurities.

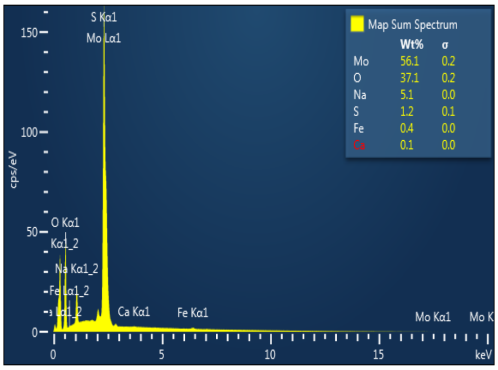

Figure 4.17: EDS spectrum of $Na_{1.9}Fe_2(MoO_4)_3Ca_{0.1}$

In Figure 4.18, the presence of sodium, Molybdenum, iron, chromium and oxygen was confirmed. The presence of sulphur which were not desired was also shown. This was due to the starting material or contamination from the furnace drying the process.

**(a)** **(b)**

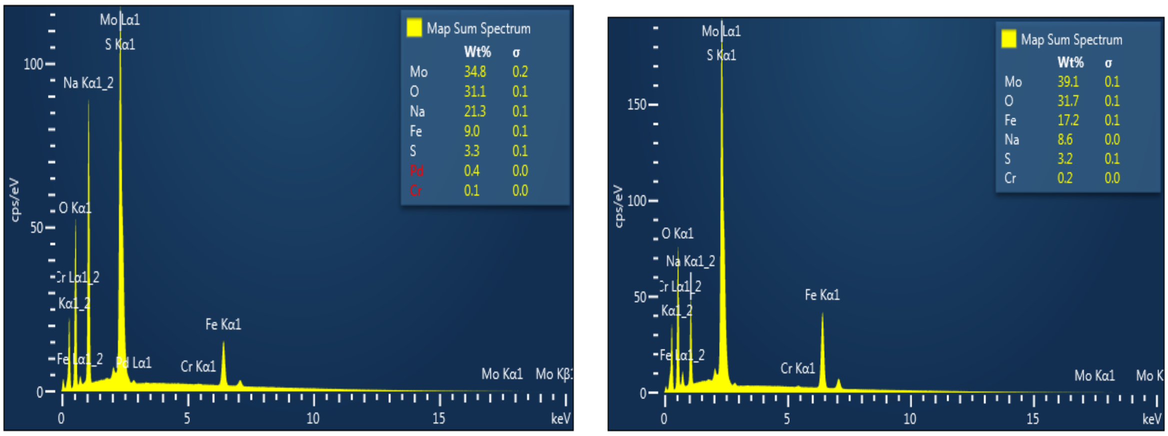

Map Sum Spectrum

| | Wt% | σ |
|---|---|---|
| Mo | 34.8 | 0.2 |
| O | 31.1 | 0.1 |
| Na | 21.3 | 0.1 |
| Fe | 9.0 | 0.1 |
| S | 3.3 | 0.1 |
| Pd | 0.4 | 0.0 |
| Cr | 0.1 | 0.0 |

Map Sum Spectrum

| | Wt% | σ |
|---|---|---|
| Mo | 39.1 | 0.1 |
| O | 31.7 | 0.1 |
| Fe | 17.2 | 0.1 |
| Na | 8.6 | 0.0 |
| S | 3.2 | 0.1 |
| Cr | 0.2 | 0.0 |

Figure 4.18 EDS spectra of (a) $Na_2Fe_{1.9}(MoO_4)_3Cr_{0.1}$ b) $Na_2Fe_{1.8}(MoO_4)_3Cr_{0.2}$

The presence of sodium, molybdenum, iron, chromium and oxygen was confirmed (Figure 4.19). The presence of sulphur which was not desired is also shown. This was due to the starting material or contamination from the furnace drying the material.

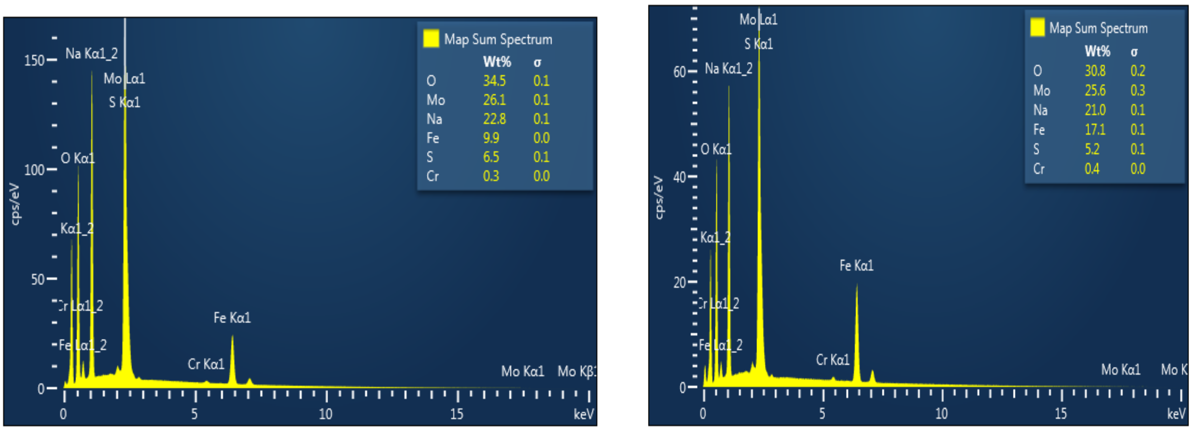

**(a)** **(b)**

Map Sum Spectrum

| | Wt% | σ |
|---|---|---|
| O | 34.5 | 0.1 |
| Mo | 26.1 | 0.1 |
| Na | 22.8 | 0.1 |
| Fe | 9.9 | 0.0 |
| S | 6.5 | 0.1 |
| Cr | 0.3 | 0.0 |

Map Sum Spectrum

| | Wt% | σ |
|---|---|---|
| O | 30.8 | 0.2 |
| Mo | 25.6 | 0.3 |
| Na | 21.0 | 0.1 |
| Fe | 17.1 | 0.1 |
| S | 5.2 | 0.1 |
| Cr | 0.4 | 0.0 |

Figure 4.19: EDS spectra of (a) $Na_2Fe_{1.7}(MoO_4)_3Cr_{0.3}$ (b) $Na_2Fe_{1.6}(MoO_4)_3Cr_{0.4}$

Figure 4.20 shows a high amount of sulphur, possibly because KCl used as a source of potassium was contaminated. The spectrum $Na_{1.8}Fe_2(MoO_4)_3K_{0.2}$ was therefore not impurity free.

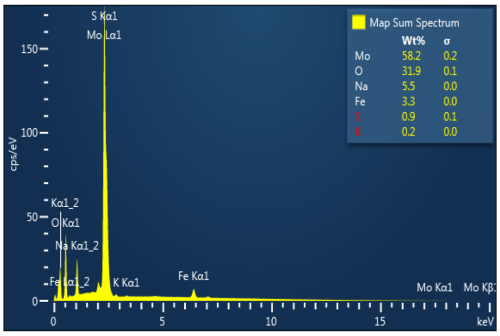

| | Wt% | σ |
|---|---|---|
| Mo | 58.2 | 0.2 |
| O | 31.9 | 0.1 |
| Na | 5.5 | 0.0 |
| Fe | 3.3 | 0.0 |
| S | 0.9 | 0.1 |
| K | 0.2 | 0.0 |

Figure 4.20: EDS spectrum of $Na_{1.8}Fe_2(MoO_4)_3K_{0.2}$

## 4.5 Fourier Transform Infrared Spectroscopy

The FTIR spectra were recorded in transmission mode in the wavenumber region ranging between 400 cm$^{-1}$ and 4000 cm$^{-1}$ (Figure 4.21). The absorption band observed at 1674.13 cm$^{-1}$ confirmed the presence of the metal oxide (Na-O) vibrational frequency, and the band at 1429.75 cm$^{-1}$ is due to the C-O stretch due to citric acid used as a chelating agent (Bassler et al., 1981). The band observed at 597cm$^{-1}$ shows the presence of copper oxide (Cu-O). The stretching band of iron oxide (Fe-O) was observed at 567 cm$^{-1}$ in spectra. The molybdenum oxide stretching band was observed at 814.77 cm$^{-1}$.

The $Na_2Fe_2(MoO_4)_3$ FTIR spectrum reveals two prominent bands at 565 and 840 cm$^{-1}$, as well as two comparatively weak bands at 421 and 967 cm$^{-1}$. The strong band at 840 cm$^{-1}$ was due to the tetrahedral $MoO_4$ units of $Na_2Fe_2(MoO_4)_3$, while the other strong bands at 565 cm$^{-1}$ were due to the bridging Mo–O–Mo bonds. The weaker bands detected at 967 cm$^{-1}$ and 421 cm$^{-1}$, on the other hand, can be attributed to the vibrational and stretching modes of Fe-O-Mo bonds. The weak bands of chromium oxide were detected at 530 cm$^{-1}$, while calcium shows a stronger vibrational stretching at 3520 cm$^{-1}$ the vibrational bands of zinc at 520 cm$^{-1}$ reflect a good crystalline quality. The K-O band stretch is not shown because the measurement was up to 500 cm$^{-1}$ frequency.

When comparing the FTIR spectra, in Figure 4.21, of the parent material $Na_2Fe_2(MoO_4)_3$ and doped material, it can be seen that, as the amount of copper increases, the band in the region 1000 - 1200 cm$^{-1}$ becomes narrower and less intense. This was due to the Cu-O bond in the doped $Na_2Fe_2(MoO_4)_3$. As the concentration of dopant increases in all spectra, the O–H band at around 3000 – 3600 cm$^{-1}$ also narrows.

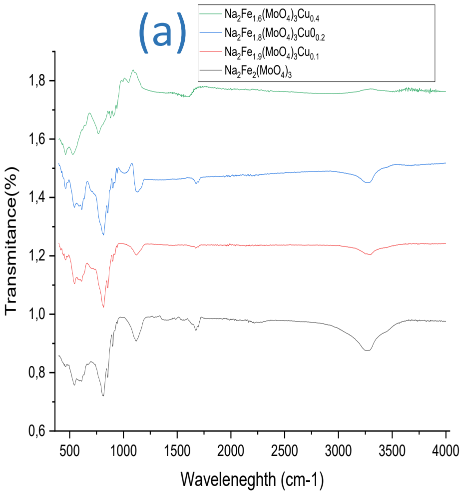
(a)
Na2Fe1.6(MoO4)3Cu0.4
Na2Fe1.8(MoO4)3Cu00.2
Na2Fe1.9(MoO4)3Cu0.1
Na2Fe2(MoO4)3
Transmitance(%)
0,6
0,8
1,0
1,2
1,4
1,6
1,8
500
1000
1500
2000
2500
3000
3500
4000
Waveleneghth (cm-1)

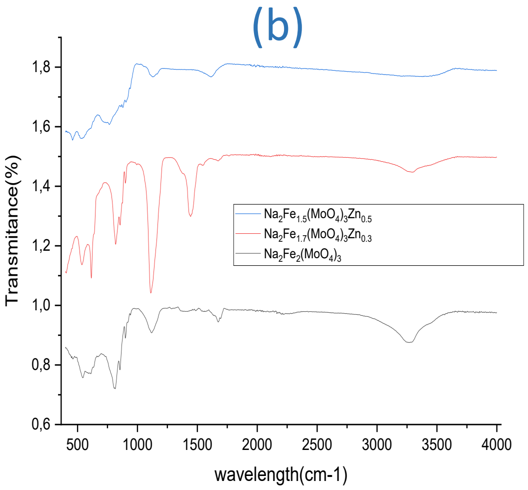
(b)
Na2Fe1.5(MoO4)3Zn0.5
Na2Fe1.7(MoO4)3Zn0.3
Na2Fe2(MoO4)3
Transmitance(%)
0,6
0,8
1,0
1,2
1,4
1,6
1,8
500
1000
1500
2000
2500
3000
3500
4000
wavelength(cm-1)

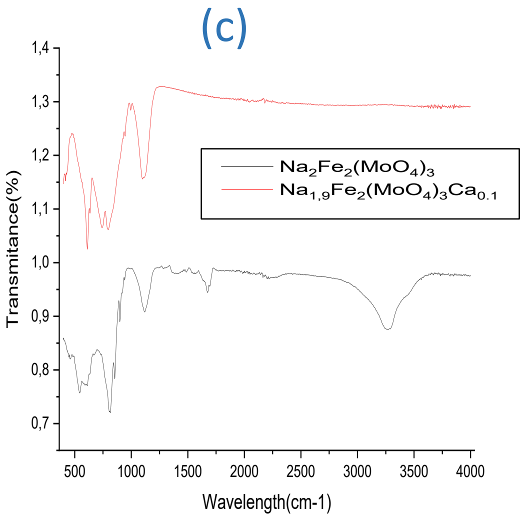
(c)
Na2Fe2(MoO4)3
Na1,9Fe2(MoO4)3Ca0.1
Transmitance(%)
0,7
0,8
0,9
1,0
1,1
1,2
1,3
1,4
500
1000
1500
2000
2500
3000
3500
4000
Wavelength(cm-1)

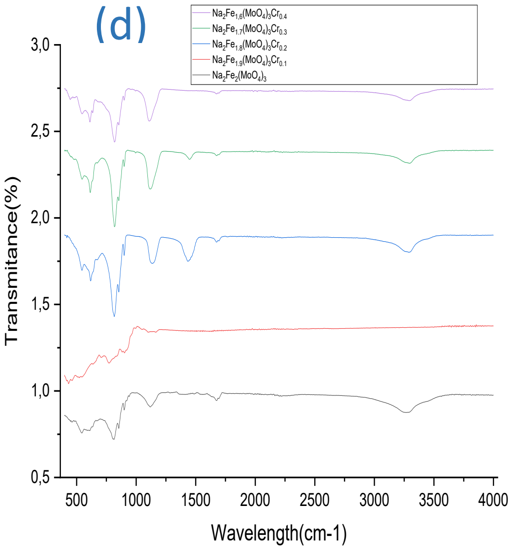
(d)
Na2Fe1,6(MoO4)3Cr0.4
Na2Fe1.7(MoO4)3Cr0.3
Na2Fe1.8(MoO4)3Cr0.2
Na2Fe1.9(MoO4)3Cr0.1
Na2Fe2(MoO4)3
Transmitance(%)
0,5
1,0
1,5
2,0
2,5
3,0
500
1000
1500
2000
2500
3000
3500
4000
Wavelength(cm-1)

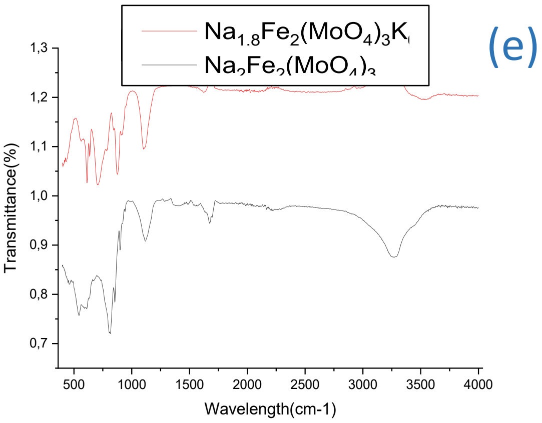

**Figure 4.21** FTIR spectra of $Na_2Fe_2(MoO_4)_3$ parent structure doped at different concentrations : (a) $Na_2Fe_2(MoO_4)_3$ doped with copper,(b) $Na_2Fe_2(MoO_4)_3$ doped with zinc, (c) $Na_2Fe_2(MoO_4)_3$ doped with calcium,(d) $Na_2Fe_2(MoO_4)_3$ doped with chromium and (e) $Na_2Fe_2(MoO_4)_3$ doped with potassium.

Table 4.6 shows the shift of bands in the FTIR spectra. When the $Na_2Fe_2(MoO_4)_3$ was doped with copper there was a shift of bands and the Cu-O vibration was introduced at 611.70 $cm^{-1}$. The Na-O bands' shifts from 1674.13 to 1676.18 $cm^{-1}$ and Mo-O from 899.46 to 899.24 $cm^{-1}$. When $Na_2Fe_2(MoO_4)_3$ was doped with zinc there was a shift of bands and the Zn-O is detected at 461.42 $cm^{-1}$. The Na-O band shifts from 1674.13 to 1700.87 $cm^{-1}$ and Mo-O from 899.46 to 876.28 $cm^{-1}$.

Table 4.6: The FTIR spectral bands of samples

| | Frequency in $cm^{-1}$ | | | | | | | |
|---|---|---|---|---|---|---|---|---|
| Samples | Na-O | Mo-O | Fe –O | Cu-O | Zn-O | Cr-O | Ca-O | K-O |
| (a) $Na_2Fe_2(MoO_4)_3$ | 1674.13 | 899.46 | 543.67 | ------------ | ------------- | ------ | -------- | ----- |
| (b) $Na_2Fe_{1.9}(MoO_4)_3Cu_{0.1}$ | 1673.37 | 900.03 | 545.31 | 611.70 | ----------- | ------ | -------- | ----- |
| (c ) $Na_2Fe_{1.8}(MoO_4)_3Cu_{0.2}$ | 1670.16 | 899.24 | 546.47 | 614.99 | ------- | --- | ----- | --- |
| (d) $Na_2Fe_{1.6}(MoO_4)_3Cu_{0.4}$ | 1676.18 | 899.27 | 540.17 | 600 | ----------- | ------ | -------- | ----- |
| (e) $Na_2Fe_{1.7}(MoO_4)_3Zn_{0.3}$ | 1600.01 | 767.29 | 527.53 | --------- | 461.42 | --- | ----- | --- |
| (f) $Na_2Fe_{1.5}(MoO_4)_3Zn_{0.5}$ | 1620.00 | 876.28 | 562.88 | -------- | 432.75 | --- | ----- | --- |

| | | | | | | | | |
|---|---|---|---|---|---|---|---|---|
| (g) $Na_2Fe_{1.9}(MoO_4)_3Ca_{0.1}$ | 1700.87 | 860.12 | 567.90 | ------- | ----------- | ------ | 3480.02 | ----- |
| (h) $Na_2Fe_{1.9}(MoO_4)_3Cr_{0.1}$ | 1689.02 | 850.03 | 514.56 | -------- | -------- | 520.12 | ---- | --- |
| (i) $Na_2Fe_{1.8}(MoO_4)_3Cr_{0.2}$ | 1600.90 | 854.28 | 546.67 | -------- | ------- | 614.67 | ----- | --- |
| (j) $Na_2Fe_{1.7}(MoO_4)_3Cr_{0.3}$ | 1434.72 | 854.36 | 545.37 | --------- | ------- | 515.40 | ----- | --- |
| (k) $Na_2Fe_{1.6}(MoO_4)_3Cr_{0.4}$ | 1530.70 | 850.80 | 544.54 | --------- | -------- | 510.03 | -------- | ------ |
| (l) $Na_{1.8}Fe_2(MoO_4)_3K_{0.2}$ | 1490.32 | 854.28 | 548.67 | --------- | -------- | ----- | ------- | 300 |

## 4.7 X-ray fluorescence Spectroscopy (XRF)

XRF provide the elemental composition of a material by determining the energy of X-rays emitted by a particular element. The XRF establishes the elemental composition of the sample and quantitatively measures the concentration of these elements. In table 5.7 $Na_2Fe_2(MoO_4)_3$ has the Fe = 9.543 and Mo = 44.003 ppm which shows that the parent structure was successfully synthesized. $Na_2Fe_{1.9}(MoO_4)_3Cu_{0.1}$ Fe = 6.178, Mo = 39.271 and Cu = 0.310 ppm. Showing the XRF concentration of elements present in the material in ppm, the drawback of using the XRF in $Na_2Fe_2(MoO_4)_3$ was that it doesn’t show the concentration of sodium. The dopants used which are copper and zinc in Table 4.7 below were successful absorbed and therefore its elemental composition was visible.

Table 4.7: The elemental composition of materials in ppm

| Element Symbol | $Na_2Fe_2(MoO_4)_3$ | $Na_2Fe_{1.9}(MoO_4)_3Cu_{0.1}$ | $Na_2Fe_{1.5}(MoO_4)_3Cu_{0.5}$ | $Na_2Fe_{1.5}(MoO_4)_3Zn_{0.5}$ | $Na_2Fe_{1.6}(MoO_4)_3Cu_{0.4}$ |
|---|---|---|---|---|---|
| Mg | 0.533 | 0.361 | 0.187 | 0.57 | 0.168 |
| Cl | 0.176 | 0.132 | 0.113 | 0.121 | 0.191 |
| $K_2O$ | 0.017 | 0.021 | 0.022 | 0.018 | 0.024 |
| $TiO_3$ | 0.013 | 0 | 0.014 | 0.014 | 0.019 |
| V | 0.01 | 0 | 0.014 | 0.121 | 0.130 |
| $Fe_2O_3$ | 9.543 | 6.178 | 10.335 | 2.795 | 9.794 |
| Cu | 0.015 | 0.310 | 0.049 | 0.002 | 0.4 |
| Zn | 0 | 0 | 0.635 | 0.56 | 0.257 |
| Zr | 0.007 | 0 | 0 | 0.006 | 0.006 |
| Nb | 0.118 | 0.104 | 0.114 | 0.105 | 0.120 |
| Ni | 0 | 0.054 | 0.098 | 0.045 | 0.081 |
| Mo | 44.003 | 39.271 | 46.250 | 39.792 | 42.598 |

When doping $Na_2Fe_2(MoO_4)_3$ at Fe site with Cr, Zn and Cu from the XRD observation when the concentration of dopants increases the crystallinity also increases hence the peaks become more sharp. When concentration incenses furthermore the peaks are shattered or cancelled off hence the peaks gets broader and smaller. When doping at Na site with K and Ca from the XRD observation the peaks become sharper and wide become smaller hence more crystal. When the concentration is increased to 0.2 the peaks become broader and the width become wider and less crystal. When doping at Na site to increase the crystallinity not more than 0.2 is required because after 0.1 the crystallinity is shattered.

SEM analysis shows that $Na_2Fe_2(MoO_4)_3$ doped at Fe site have the angular and rod shaped hence they are refer to as irregular shaped and $Na_2Fe_2(MoO_4)_3$ doped at Na site have only the rod shape.

# Chapter 5: Conclusion

$Na_2Fe_2(MoO_4)_3$ was successfully doped at the Fe and Na sites using stoichiometric amounts of reactant using a one pot sol-gel synthesises method followed by calcination in the presence of air for 3 hours at 600 °C. The structures and morphology of the samples were characterised by XRD, XRF, Raman spectroscopy, FTIR, and SEM-EDS microscopy. A few important observations of the research are discussed below:

The XRD data revealed the crystallinity of synthesized cathode materials, Doped alkali metal cations entered into the lattice successfully and this resulted in an expanded lattice. Doping with alkali cations showed a slight increase in crystallite size as the concentration of the dopant increased. For a good battery property the cathode material must be crystalline.

FTIR spectroscopy was used to confirm the presence of metal oxides in the spectra to make assure that all the metal a present on the sample. From the FTIR analysis, one distinct strong absorption band associated with the stretching mode of molybdenum oxide was observed at 900 $cm^{-1}$. Compared with the parent material, the FTIR bands for the doped metal complexes were shifted slightly towards the lower wavenumber.

In the Raman analysis, Raman peaks associated with the stretching vibrations were observed for all synthesized powder materials. Doping of $Na_2Fe_2(MoO_4)_3$ with different concentrations of metal ions does not introduce new intense Raman peaks. The peaks introduce around 1000 $cm^{-1}$ did not showany effect on the synthesised $Na_2Fe_2(MoO_4)_3$ and its dopants.

From the SEM it can be observed that the samples were less agglomerated (smaller particles) suggesting that the prepared samples may have better electrochemical performance. The results agree with those of XRD because the smaller the particles the more crystallinity. The electrochemical performance significantly depend on the material with which they were made specifically on their surface area. The twelve synthesized and characterized materials was more and less crystalline as indicated by the tables because some indicated the decomposed shuttering of crystalinity after doping.

The shapes of particles in all twelve samples were irregular and rod shape. The particle has smooth surfaces, but particle size was not uniformly distributed over the range from 1 μm - 2 μm. When the particle have the same homogeneity and the particle size is larger than it will deliver the highest initial charge capacity but its cycle life will be poor, but the smaller particle will deliver high initial capacity because it has volume of intercalation and deintercalation. The uniformity and size of particles of the electrode materials often play an important role in improving the electrochemical properties.

## 6. References

- Armand, M.,Tarascon, J, *M.Nature*,**2008**,451,652 – 653.
- Ball, D. W. Field guide for spectroscopy. (1st ed). *SPIE Publication, Bellingham.* **2006**, 5 - 9.
- Bommier, C, Ji, X.,Electrolytes, Small,. **2018,**14,1703576**.**
- Bruce, P. G., Miln, G. *J. Solid State Chem*. **1990**. 89, 162 - 166.
- Ding, J.J., Zhou,Y.N., Sun, Q., Yu, X. Q., Yang, X. Q., Fu, Z. W. *Electrochim. Acta* **2013**, 87,388 – 390.
- Dunn, B., Kamath, H., Tarascon, J. M.. *Sci* **2011**, *334*, 928 - 935.
- Dutrow, B. L., Clark, C. M. *Geo Instru- Anal*, **2011**, 12, 390 - 670.
- Ellis, B.L. & Linda, N. F. *J. Solid State Chem.* ***2012,*** 16, 168 - 169.
- Erickson, E. M., Ghanty, C., Aurbach, D. *J. Phys. Chem. Lett.* **2014**, *5*, 3313 - 3324.
- Hoffert, M. I., Caldeira, K., Benford. G., Criswell, D. R., Green. C., Herzog. H., Jain. A. K., Kheshgi. H .S., Lackner. K. S., Lewis. J. S. *Science*. **2002**, 298, 981 - 986.
- Islam,M.S., Fisher ,C. A. J. Chem.Soc.Rev.2014,43,185 – 186.
- Ji, W., Huang, H., Zhang, X., Zheng, D., Ding, T., Lambert, T.H., Qu, D. *Nano Energy.* **2020**, 72, 104705.
- Jian, Z. L., Zhao,L., Pan, H., Hu,S.Y., Li,H., Chen,W., Chen,Q.L. *Electrochem Commun.* **2012**, 14, 86 - 90.
- John, S., Newman, K. E., Thomas, A., Electrochemical systems (3rd ed). *Wiley-IEEE Press*. **2004**, 660 - 667.
- Kang, B., Cedar, G. *Nature.* **2009**, 458, 190 – 197.
- Kim,D.H., Seo,X.H., Ma,G., Cecer, K. Kang, K.W. *Adv.Energy Mater.***2012**,2, 710 – 713.
- Kundu,D., Talaie,E., Duffort,V., Nazar, L.F. Angew. Chem., *Int. Ed*. **2015**, 54, 3431 – 3432.
- Kurilchik, S., Loiko, P., Yasukevich. A., Vilejshikova, E., Serres, J.M., Mateo, X., Kisel, V., Pavyuk, A., Trifonov, V., Kuleshov, N., *J. Opt. Soc. Am*. **2017**, 1 - 2.
- Li, L. L., Xu, Y. H. *Nano Lett.,* **2012,** 12, 5664 - 5665.
- Loiko, P., Vilejshikova, E. V., Volokitina, A. A., Trifonov, V. A., Serres, J. M., Mateos, X., Kuleshow, N. V., Yumashev, K. V., Baranov, A. V., Pavyuk, A. A., *J. Lumin*. **2017**, 188, 154 - 161.
- Lu, L., Han, X.,Li, J., Hua,J., Ouyang,M.J. *Power Source*. **2013**, 226, 272 – 275.
- Manthiram, A., Goodenough, J. B J. *Solid State Chem*. **1987**, 71, 349 - 360.

- Masquelier, C., Croguennec, L., *Chem. Rev.* **2013**, *113*, 6552 - 6591.
- Meng, Y. S., Arroyo-de Dompablo, M. E. **2011**,46.
- Michae., M.S., Fauzi, A., Prabaharan, S. R. S. *Inter. J. Inorg. Mater.* **2000,** 2, 261 - 262.
- Mingzhe, C., Cortie, D., Zhe, H., Huile, K., Shun, W., Qinfen, G., Weibo, H., Wang, E., Weihong, L., Lingnu, C., Shulei, C., Xiao, L. W., Shixue, D. *Adv. Energy Mater*. **2018**, 8, 27 - 30.
- Mu,L.Q., Xu,S.Y., Li,Y.M.,Li,H., Chen,L.Q., Huang,X.J.*Adv.Mater*. **2015**, 27, 6928 – 6929.
- Muessig, E., Bramnik, K, G., Ehrenberg, H., *Acta Cryst. B.* **2003,** 59, 611 - 612.
- Myung, S.T.,Yoon,C.S., Lu,J., Hasson,J., Scrosati,B., Amine,K., Sun,Y,K. **2014**,14,1620 – 1621.
- Nadiri, A., Delmas, C., Salmon, R., Hagenmuller. P., *Rev. Chim. Minérale*. **1984**, 21, 537 - 544.
- Nanjundaswam, K. S., Padhi, A. K., Goodenough, J. B., Okada, S., Ohtsukab, H., Arai, H., Yamaki, J., *S. State Ion* .**1996**, 92 - 95.
- Padh,A.K., Manivannam,V., Goodenough,J.B., *J.Electrochem.Soc*. **1998**, 145, 1518 – 1520.
- Palomares, V., Serras, P., Villaluenga, I., Hueso, K. B., Carretero-Gonzalez, J., Rojo, T., *Energy Environ. Sci.* **2012**, *5*, 5884 - 5886.
- Pan, H.L., Hu,Y,S. *Chem. Energy Environ. Sci.* **2013**, 6, 2338 – 2339.
- Park, Y. J., Kim, J. G., Kim, M. K., Kim, H. G., Chung, A. T., Park, Y., *J. Power Sources*. ***2000*,** 87, 1, 69 - 77.
- Peters, J., Buchholz, D., Passerini, S., Weil, M. *Energy Environ. Sci.* **2016**, 9, 1744 - 1745.
- Saiful Islam, M & Fisher .C, A, J. *Chem. Soc. Rev.* **2014,** 43**,** 185 - 187.
- Shen, W., Wang, W., Liu, H. M., Yang, W. S., *Chem.: Eur. J.* **2013**, 43, 14712 - 14713.
- Shirakawa, J., Nakayama, M., Wakihara, M. & Uchimoto, Y., *J Phys. Chem.* B. **2007**, 111, 1424 - 1430.
- Shirakawa, J., Nakayama, M., Wakihara, M., Uchimoto, Y., *J. Phys. Chem. B*.**2006**, 110, 17743 - 17750.
- Shuai, M., Wen, S., *PRO NAT SCI-Matter*. **2018**, 28, 6, 653 - 666.
- Slater, M. D., Kim, D. H., Lee, E., Johnson, C. S. *Adv. Funct. Mater.* ***2013*,** 23, 947 - 948.

- Smit, P. J., Poeppelmeier, K. R., Stair, P. C.. *J. Solid. State. Chem*. **2006,** 12, 23, 5944 - 5953.
- Sun, J., Lee, H.W., Pasta, M., Yuan, H., Zheng, G., Sun, Y., Li, Y., Cui, Y. *Nat.Nanotechnol*. **2015**, 10, 980 – 983.
- Sun, Q., Ren, Q. Q., Fu, Z. W., *Electrochem. Commun*. **2012**, 23, 145 - 148.
- Sun, Y., Zhao, L., Pan, H., Lu, X., Gu, L., Hu, Y. S., Li, H., Armand, M., Ikuhara, Y., Chen, L. *Nat. Commun*. **2013**, 4, 1870 - 1871.
- Tarascon, J. M., Armand, M. *Nature.* **2001**, 414, 359 - 360.
- Trad, K and Carlier,D. *J. Phys. Chem. C*. **2010**, 114. 10034 - 10035.
- Wang, L. P., Yu, L., Wang, X., Srinivasan, M., Xu, Z. J. *J. Mater. Chem*. **2015**, 3, 9353 - 9378.
- Wang. W., Jiang, B., Hu, L. W., Lin, Z .S., Hou, J. G., Jiao, S. Q., *J. Power Sources*. **2014**, 250, 181 – 182.
- Whittingham, M. S., *Chem. Rev.* **2014**, *114*, 11414 - 11443.
- Xu, B., Qian, D., Wang, Z., Meng, Y. S., *Mater. Sci. Eng. Reports*. **2012**, 73, 51 - 65.
- Yabuuchi, N., Kubota, K., Dahbi, M. S., Komaba, L. *Chem. Rev*. **2014**, 114, 11636 - 11637.
- Yu, C. Y., Park, J.S., Jung, H.G., Chung, K.Y., Aurbach, D., Sun, Y.K, Myung, S.T. *Energy Environ.Sci*. **2015**, 8, 2018 – 2019.
- Yue, J.L., Zhou, Y.N., Shi, S.Q., Shadike, Z., Huang, X-Q., Luo, J., Yang, Z.Z., Li, H., Gu, L., Yang, X-Q., Fu, Z-W., *Sci. Rep.* **2015***, 5*, 8810
- Zheng, Y., Zhang, P., Wu, S. Q., Wen, Y. H., Zhu, Z. Z., Yang, Y., *J. Electrochem. Soc.* **2013**,160, 927 - 928.
- Zhi, M, Xiang, C., J. Li, M. Li and N. Wu, *Nanoscale.* **2013**, 5, 72 - 73
- Zhou, S., Barim, G., Morgan, B. J., Melot, B.C., R.L. Brutchery., *Chem. Mater.* **2016**,28(12),4492 – 4500.